

## Compressibility effects of supersonic Batchelor vortices

Toshihiko Hiejima \*

*Department of Aerospace Engineering, Osaka Prefecture University, 1-1 Gakuen-cho,  
Nakaku, Sakai, Osaka 599-8531, Japan*



(Received 6 May 2019; published 16 September 2019)

Transition processes in supersonic Batchelor vortices with small disturbances are investigated numerically at Mach numbers 1.5–5.0. The Batchelor vortices for isentropic and uniform stagnation-temperature vortices are considered in terms of thermodynamic properties. In the evolutions, the former vortices are not influenced by compressibility effects; however, the latter have demonstrated slow growth as the Mach number increases. Compressibility effects primarily mean that fluctuation growth related to turbulence is suppressed as the Mach number increases. In spatial fluctuation energy production, isentropic vortices exhibit only kinetic energy fluctuations and uniform stagnation-temperature vortices cause large entropy fluctuation energy with increasing the Mach number. When the Mach number is large, the kinetic fluctuation energy is greatly decreased and the increase in entropy fluctuations is associated with reduced kinetic fluctuation energy. In addition, it is found that the entropy fluctuation property at uniform stagnation temperatures is consistent with the expression derived from the kinetic fluctuation energy based on Morkovin's hypothesis. The present results support the notion that the coefficient of variation of density is appropriate to evaluate compressibility effects. Entropy fluctuation generalizes fluctuation of thermodynamic quantity such as density fluctuation. Therefore, it follows that the property of entropy is strongly related to intrinsic compressibility.

DOI: [10.1103/PhysRevFluids.4.093903](https://doi.org/10.1103/PhysRevFluids.4.093903)

### I. INTRODUCTION

In high-speed flows, turbulence structures are strongly affected by compressibility. The spreading rate of a shear layer decreases sharply as the Mach number increases because compressibility inhibits the entrainment of mass and turbulent diffusion. Early studies suspected that the density ratio between the two streams in shear layers caused the reduced growth rate. However, for various density ratios, Brown and Roshko [1] showed that reduced spreading rates were due to compressibility effects and should not be attributed solely to the density ratio. Bogdanoff [2], Papamoschou and Roshko [3] introduced the notion of convective Mach number  $M_c$  as a parameter that can determine compressibility effects effectively. From flow visualisations, Clemens and Mungal [4] observed that large-scale coherent structures in a shear layer change as the  $M_c$  increases. Although the  $M_c$  parameter could successfully estimate compressibility, it has also been pointed out that the compressibility parameter may not be sufficient because the spreading rates organized by the convective Mach number  $M_c$  demonstrate significant scatter [5]. Based on multiple shear layer measurements, Slessor *et al.* [6] proposed a way to correct scattering in the spreading rate relative to a convective Mach number by introducing another compressibility parameter. Barre *et al.* [7] pointed out that the anisotropy of turbulent stresses appeared to be affected by compressibility. Vreman *et al.* [8] showed that compressibility effects are reflected in pressure-strain correlations and

---

\*hiejima@aero.osakafu-u.ac.jp

the Reynolds stress anisotropy tensor. They proposed a model for the reduced pressure fluctuations that considered the anisotropy effect. For shear flows, Pantano and Sarkar [9] demonstrated that as the  $M_c$  increases, the pressure-strain term decreases, which lead to inhibited energy transfer from streamwise to cross-stream fluctuations.

Compressibility studies have focused extensively on turbulent boundary layers and shear flows [10–14]. According to Morkovin’s hypothesis [12], compressibility effects do not become important until the fluctuating Mach number exceeds 0.3, which is equivalent to a freestream Mach number of approximately four. Moreover, the turbulence structure is closely related to that in the corresponding constant-density flow, i.e., incompressible flow. For supersonic flows with moderately high Mach numbers, the direct effects of compressibility on wall turbulence at zero pressure gradients are small and significant differences occur due to variations in the thermodynamic properties across the layer. Duan *et al.* [15] stated that the possible effects of compressibility are reflected by increasing fluctuations of thermodynamic quantities. For example, density fluctuations greater than 5% were measured in supersonic turbulent boundary layers at Mach number 3.0 [16]. If the root-mean-square density fluctuation is not large compared to the absolute density in the boundary layers and wake flows below Mach number 5, or jet flows below Mach number 1.5, the effects of density fluctuations on turbulence are small with a steady pressure distribution [10]. However, fluctuations of thermodynamic quantities and turbulent Mach numbers increase dramatically when the freestream Mach number increases [14].

Gerolymos and Vallet [17] investigated fluctuations of thermodynamic variables in compressible turbulent plane channel flow. They stated that the coefficient of variation of density  $\hat{\rho}/\bar{\rho}$  (the ratio of the standard deviation to the mean) is the optimal measure of compressibility effects on turbulence and that the dilatational terms are often negligible. Moreover, using supersonic and incompressible heated boundary layers, Liu and Pletcher [18] studied the effects of density fluctuation and profile on compressibility. They found that both compressibility and density profile effects satisfied the similarity laws for the boundary layer profile and that the density profile effect influences density fluctuation significantly. Although there is a close relationship between compressibility, variable density profile and density fluctuation, the explicit relation in compressible flows has not been clarified.

In thermodynamic quantities, entropy changes are fundamental. Density fluctuations are closely related to entropy (temperature) fluctuations. Goldstein [19] investigated analytically the turbulence generated by the interaction of random entropy fluctuations with nonuniform mean flows and demonstrated that the energy of entropy-generated turbulence increases much more rapidly with a contraction ratio than that of imposed upstream turbulence. From an integration of the mean entropy equation, Lele [11] indicated that increased entropy and the associated total pressure loss may be significant at moderate and high convective Mach numbers. Therefore, the relation between entropy fluctuations and turbulence must also be considered to elucidate compressibility effects.

In terms of compressibility effects, the following shear flows define the significance of streamwise vorticity. Schadow *et al.* [20] studied the compressible spreading rates of supersonic coaxial jets for circular and rectangular inner jets. They found that the spreading rates varied with the convective Mach number in a manner similar to plane shear layers and that the rectangular jet was superior to the circular jet relative to spreading rate. Apparently, the increase of spreading rate is considered to be due to streamwise vortices generated from the rectangular geometry. It is known that naturally developing, three-dimensional structures (streamwise vortical structures) enhance the growth rate of the turbulent mixing layer [11]. Experimental and numerical investigations [21–23] suggest that streamwise vortices have a high mixing performance in supersonic flows that is connected to relaxation of compressibility effects. The property of the vortices can also be inferred from the growth of three-dimensional waves in shear layers, which reduce compressibility beyond the convective Mach number 0.6 [24]. In fact, compressible streamwise vortices originally develop as three-dimensional waves with a fast growth rate and possess variable thermodynamic (pressure, density and temperature) profiles that increase the propensity for fluctuation growth. Note that the

compressibility effect, i.e., vortical activity suppression, differs from acoustic modes [25], which grow stronger as the Mach number increases.

As mentioned above, streamwise vortices have shown promise as a way to reduce compressibility effects and produce supersonic turbulence (fluctuation growth). However, to date, few studies have investigated the mechanism for compressibility of streamwise vortices. In terms of streamwise vorticity and based on a few experiments, Naughton *et al.* [26] considered a compressibility effect of swirling flows and demonstrated that the growth rate of swirling jets was greater than that of nonswirling counterparts. According to linear stability analysis of streamwise vortices with uniform stagnation temperatures [27], the greater the Mach number, the larger the density fluctuation. In contrast to boundary layers and shear flows, in nonlinear developments of streamwise vortices, the mechanism of the reduced spreading rate remains unclear. Similar to the vortices, how compressibility effects are caused by a nonuniform thermodynamic profile has not been clarified. Therefore, as a step toward understanding of universal compressibility effects, it is important to know the fluctuation feature through the evolution of streamwise vortices, which, unlike boundary layers and shear flows that are nearly parallel flows, are associated with a nonuniform pressure profile.

In previous works, supersonic Batchelor vortices at uniform stagnation temperatures have been studied in terms of linear stability analysis [27], direct numerical simulation [28,29] and vortex breakdown [30,31]. The present study investigates the effects of variable thermodynamic properties on spatial evolution and compressibility effects in a supersonic Batchelor vortex as a streamwise vortex, which is important to clarify the fundamental physics in high-speed flows. Many vortical flows have been interpreted using linear stability theory and nonlinear simulations. In this study, the spatial evolutions of streamwise vortices with linear unstable modes and random disturbances are investigated numerically for two types of thermodynamic conditions under the theme of fluctuation growth.

The remainder of this paper is organized as follows. In Sec. II, the numerical method and computational conditions, including the use of supersonic Batchelor vortices as inflow conditions, are described. In Sec. III, the results of spatial development of linear unstable modes are provided and discussed. Based on a detailed analysis of fluctuation energies, how effective entropy fluctuation is on the compressibility of vortices developed by varying Mach numbers is shown in Sec. IV using linear unstable and random disturbances. Conclusions and suggestions for future work are presented in Sec. V.

## II. NUMERICAL FORMULATIONS

### A. Nondimensionalization of physical variables

The dimensional density, three velocity components, pressure, temperature, and entropy are denoted  $\rho^*$ ,  $u_i^*$ ,  $p^*$ ,  $T^*$  and  $s^*$ , respectively. The reference length of a Batchelor vortex is defined as  $\delta_s^*$  that denotes the swirl thickness obtained from  $\Gamma^* = (\pi \delta_s^*) \omega_{x,\max}^*$ , where  $\omega_{x,\max}^*$  denotes the maximum axial vorticity and  $\Gamma^*$  represents the total circulation of the entire distributed axial vorticity. By using the freestream sonic velocity  $c_\infty^* (= \sqrt{\gamma R^* T_\infty^*})$  and density  $\rho_\infty^*$ , the physical variables can be normalized as follows:

$$\rho = \frac{\rho^*}{\rho_\infty^*}, \quad u_i = \frac{u_i^*}{c_\infty^*}, \quad p = \frac{p^*}{\rho_\infty^* c_\infty^{*2}}, \quad T = \frac{T^*}{\gamma T_\infty^*}, \quad s = \frac{s^*}{C_v^*}, \quad r = \frac{r^*}{\delta_s^*}, \quad x = \frac{x^*}{\delta_s^*}, \quad t = \frac{c_\infty^*}{\delta_s^*} t^*, \quad (1)$$

where  $\gamma$  is the ratio of the specific heats,  $R^*$  is the gas constant,  $T_\infty^*$  is the freestream temperature and  $C_v^* = R^*/(\gamma - 1)$  represents the specific heat at a constant volume, because, in a perfect gas containing simple molecules, specific heat is constant over a wide temperature range. Here the freestream Mach number  $M_\infty$  and Reynolds number  $Re$  are defined as

$$M_\infty = \frac{U_\infty^*}{c_\infty^*}, \quad Re = \frac{\rho_\infty^* U_\infty^* \delta_s^*}{\eta_\infty^*}, \quad (2)$$

where  $U_\infty^*$  is the freestream velocity and  $\eta_\infty^*$  is the viscosity.

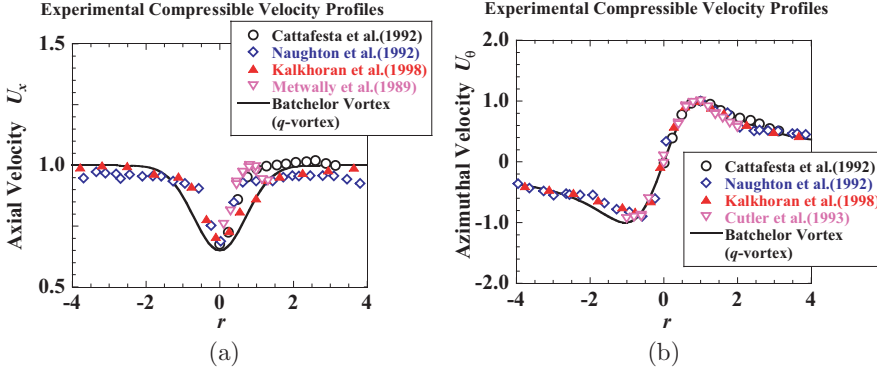


FIG. 1. Comparison of Batchelor vortex profiles with experimental measurements in supersonic streamwise vortices for (a) axial velocity and (b) azimuthal velocity. Reprinted with permission from T. Hiejima, *Phys. Fluids* **25**, 114103 (2013). Copyright 2013 American Institute of Physics.

### B. Supersonic Batchelor vortex

To study the compressibility effects of supersonic streamwise vortices, Batchelor vortices [32] are used under supersonic flows because their profiles are compatible with many experimental swirling flows at high Reynolds numbers, as shown in Fig. 1. The radial, azimuthal, and axial velocities ( $u_r$ ,  $u_\theta$ , and  $u_x$ , respectively) of the Batchelor vortex are given as follows:

$$u_r(r) = 0, \quad u_\theta(r) = M_\infty \frac{q}{r} [1 - \exp(-r^2)], \quad u_x(r) = M_\infty [1 - \mu \exp(-r^2)], \quad (3)$$

where  $q$  and  $\mu$  denote the swirl intensity (circulation) and axial velocity deficit, respectively. For incompressible streamwise vortices, the linear growth rate increases as the swirl increases [33,34]. In contrast, in supersonic flows, it is difficult to generate a streamwise vortex with a strong swirl (i.e., large circulation) due to the incidence shockwave or separation on a device. According to devices generating a Batchelor-type vortex in supersonic flows [26,35], the maximum swirl intensity is approximately  $q \sim 0.2$ . Here  $q = 0.16$ . It has also been shown that the fluctuation growth of the vortex with a large swirl is weak due to rotational stabilisation [28,36,46]. The axial velocity deficit is roughly 0.5–0.8 because a flow behind the devices that generated the vortex is similar to a wake flow. Note that, in Fig. 1, the deficit  $\mu \approx 0.3$  because the measured points are set downstream far from the devices; however, the axial velocity profiles recover the deficit in the wake flows.

The normalized entropy equation is defined as

$$s = \log \left( \frac{p}{\rho^\gamma} \right) + \text{const.} \quad (4)$$

At high Reynolds numbers, the mainstream flows do not appreciably depend on viscosity; hence, they can reasonably be regarded as inviscid supersonic flows. Using the radial momentum equation and the derivation of the entropy definition Eq. (4), the density  $\rho(r)$  and pressure  $p(r)$  required for compressible flows in basic inviscid steady flow are given as follows:

$$\frac{dp}{dr} = \rho \frac{u_\theta^2}{r}, \quad \frac{d\rho}{dr} = \frac{\rho}{\gamma} \left( \frac{1}{p} \frac{dp}{dr} - \frac{ds}{dr} \right). \quad (5)$$

The Crocco equation is expressed as follows:

$$\frac{1}{\gamma - 1} T \frac{ds}{dr} = \frac{\gamma}{\gamma - 1} \frac{dT_0}{dr} - u_\theta \omega_x + u_x \omega_\theta, \quad (6)$$

TABLE I. Eigenvalues of unstable modes obtained from compressible linear stability analysis at  $M_\infty = 2.5$ ,  $q = 0.16$ , and  $\mu = 0.5$ .

Inflow Batchelor vortex	$-\alpha_r$	$-\alpha_i$	$m$	$\omega/M_\infty$
Isentropic condition	0.74407	0.16023	-1	0.583
Isentropic condition	0.74957	0.15633	-2	0.745
Isentropic condition	0.83186	0.15427	-3	0.938
Isentropic condition	0.96355	0.15439	-4	1.160
Isentropic condition	1.11657	0.15502	-5	1.395
Isentropic condition	1.28088	0.15572	-6	1.637
Uniform stagnation temperature	0.67001	0.14040	-1	0.562
Uniform stagnation temperature	0.68514	0.12691	-2	0.718
Uniform stagnation temperature	0.78638	0.12295	-3	0.918
Uniform stagnation temperature	0.92943	0.12181	-4	1.145
Uniform stagnation temperature	1.08770	0.12153	-5	1.382
Uniform stagnation temperature	1.25647	0.12155	-6	1.626

where  $\omega_x$  and  $\omega_\theta$  are the axial and azimuthal vorticities, respectively. For the entropy gradient in Eq. (5), one case is described by Eq. (6), assuming that the stagnation temperature  $T_0$  is uniform. The other case is derived from an isentropic condition, i.e.,  $ds/dr = 0$ ; here, it means a uniform entropy.

### C. Linear stability analysis

The linear disturbance is represented as  $\phi(r) \exp[i(\alpha x + m\theta - \omega t)]$ , the eigenfunction is  $\phi(r) = \{R, U, V, W, P, \Omega_x\}$ , where  $R, U, V, W, P$ , and  $\Omega_x$  denote the density, radial velocity, azimuthal velocity, axial velocity, pressure, and axial vorticity disturbances, respectively. Here the axial wave number is  $\alpha_r$ , the growth rate is  $-\alpha_i$  ( $\alpha = \alpha_r + i\alpha_i$ ; complex), the azimuthal wave number (integer) is  $m$ , the frequency (real) is  $\omega$ . Inviscid linearized disturbance equations are derived as second order ordinary differential equations. A shooting method is used to solve the complex eigenvalue  $\alpha$  and the eigenvalues for the maximum growth rate are listed in Tables I and II. The previous study provides details about the eigenvalue problem solution [27].

 TABLE II. Eigenvalues of unstable modes obtained from compressible linear stability analysis at  $M_\infty = 5.0$ ,  $q = 0.16$ , and  $\mu = 0.5$ .

Inflow Batchelor vortex	$-\alpha_r$	$-\alpha_i$	$m$	$\omega/M_\infty$
Isentropic condition	0.62707	0.12618	-1	0.501
Isentropic condition	0.70971	0.14535	-2	0.710
Isentropic condition	0.81857	0.14955	-3	0.923
Isentropic condition	0.95553	0.15173	-4	1.150
Isentropic condition	1.11323	0.15329	-5	1.398
Isentropic condition	1.27964	0.15450	-6	1.633
Uniform stagnation temperature	0.51812	0.09795	-1	0.476
Uniform stagnation temperature	0.59555	0.09009	-2	0.662
Uniform stagnation temperature	0.72954	0.08741	-3	0.881
Uniform stagnation temperature	0.88176	0.08605	-4	1.113
Uniform stagnation temperature	1.03914	0.08526	-5	1.349
Uniform stagnation temperature	1.20055	0.08480	-6	1.588

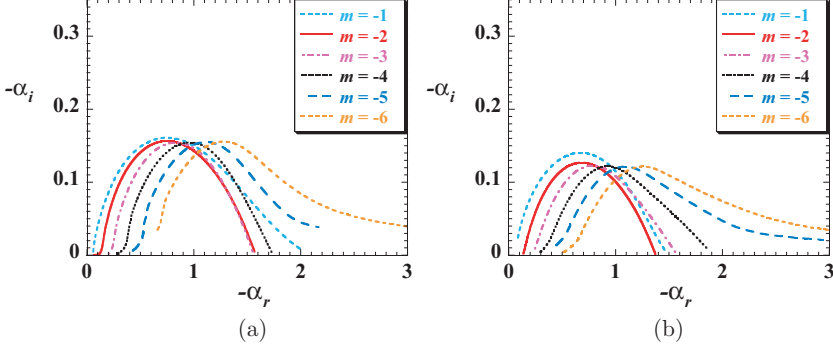


FIG. 2. Relations between the growth rate and the axial wave number,  $-\alpha_i$  vs.  $-\alpha_r$ , obtained from linear stability theory at  $M_\infty = 2.5$ ,  $q = 0.16$  and  $\mu = 0.5$ ; (a) isentropic condition, (b) uniform stagnation temperature.

The linear disturbance of the Bachelor vortex were obtained from the linear stability analysis. Figure 2 shows the growth rate  $-\alpha_i$  as a function of  $-\alpha_r$  for  $q = 0.16$  and  $\mu = 0.5$  at  $M_\infty = 2.5$ . The result shows that the maximum growth rate of isentropic vortices is larger than that of uniform stagnation temperature vortices and the axial wave number  $-\alpha_r$  increases as the azimuthal wave number  $-m$  increases under both the thermodynamic conditions. In other words, briefly  $-\alpha_r$  is proportional to  $-m$  on the most unstable mode; note that in shear layers the instability characteristics is often expressed by the relation between  $\alpha_r$  and  $-\alpha_i$ . Thus, the properties of developing vortices can be observed by focusing on the azimuthal wave number.

#### D. Governing equations

The normalized governing equations are the three-dimensional, unsteady, compressible Navier-Stokes equations in the general coordinates  $\xi_i$  ( $i = 1-3$ ), which are given as

$$\frac{\partial}{\partial t} \left( \frac{\mathbf{Q}}{J} \right) + \frac{\partial \mathbf{F}_i}{\partial \xi_i} = \frac{\partial \mathbf{F}_{vi}}{\partial \xi_i}, \quad (7)$$

$$\mathbf{Q} = \begin{bmatrix} \rho \\ \rho u_1 \\ \rho u_2 \\ \rho u_3 \\ e \end{bmatrix}, \quad \mathbf{F}_i = \begin{bmatrix} \rho U_i \\ \rho u_1 U_i + p (J^{-1} \partial \xi_i / \partial x_1) \\ \rho u_2 U_i + p (J^{-1} \partial \xi_i / \partial x_2) \\ \rho u_3 U_i + p (J^{-1} \partial \xi_i / \partial x_3) \\ (e + p) U_i \end{bmatrix}, \quad \mathbf{F}_{vi} = \begin{bmatrix} 0 \\ \tau_{1k} (J^{-1} \partial \xi_i / \partial x_k) \\ \tau_{2k} (J^{-1} \partial \xi_i / \partial x_k) \\ \tau_{3k} (J^{-1} \partial \xi_i / \partial x_k) \\ \beta_k (J^{-1} \partial \xi_i / \partial x_k) \end{bmatrix},$$

$$J^{-1} = \frac{\partial x_1}{\partial \xi_1} \left( \frac{\partial x_2}{\partial \xi_2} \frac{\partial x_3}{\partial \xi_3} - \frac{\partial x_2}{\partial \xi_3} \frac{\partial x_3}{\partial \xi_2} \right) + \frac{\partial x_1}{\partial \xi_2} \left( \frac{\partial x_2}{\partial \xi_3} \frac{\partial x_3}{\partial \xi_1} - \frac{\partial x_2}{\partial \xi_1} \frac{\partial x_3}{\partial \xi_3} \right) + \frac{\partial x_1}{\partial \xi_3} \left( \frac{\partial x_2}{\partial \xi_1} \frac{\partial x_3}{\partial \xi_2} - \frac{\partial x_2}{\partial \xi_2} \frac{\partial x_3}{\partial \xi_1} \right),$$

where  $\mathbf{Q}$  is a vector of conservative variables, and  $\mathbf{F}_i$  and  $\mathbf{F}_{vi}$  contain the convective and viscous fluxes, respectively. The Jacobian  $J$  transforms the coordinate system from a physical space to a computational space.  $J^{-1} \partial \xi_i / \partial x_k$  are the derivatives of the coordinate conversion, i.e., the metrics. The thermodynamics relation, the normalized equation of state and the transport coefficients are

expressed as follows:

$$\begin{aligned}
 e &= \frac{p}{\gamma - 1} + \frac{1}{2} \rho u_k u_k, \quad p = \rho T, \\
 \tau_{ij} &= \frac{\eta(T)}{\text{Re}_M} \left( \frac{\partial u_i}{\partial x_j} + \frac{\partial u_j}{\partial x_i} - \frac{2}{3} \delta_{ij} \frac{\partial u_k}{\partial x_k} \right), \quad \beta_i = u_k \tau_{ik} + q_i, \\
 q_i &= -\frac{\gamma}{(\gamma - 1)} \frac{\eta(T)}{\text{Re}_M \text{Pr}} \frac{\partial T}{\partial x_i}, \quad U_i = \left( J^{-1} \frac{\partial \xi_i}{\partial x_k} \right) u_k,
 \end{aligned} \tag{8}$$

where  $e$  is the total energy,  $\tau_{ij}$  is the viscous stress tensor,  $q_i$  is the conductive heat flux,  $U_i$  are the velocity components at the cell interface, and  $u_i$  are the velocity components in Cartesian coordinates. The Reynolds number based on the sonic velocity is defined as  $\text{Re}_M = (\rho_\infty^* c_\infty^* \delta_s^*) / \eta_\infty^*$  ( $= \text{Re} / M_\infty$ ), and the Prandtl number  $\text{Pr} = 0.72$ . The viscosity  $\eta$  is calculated from Sutherland's law,

$$\eta(T) = T^{\frac{3}{2}} \frac{1 + \vartheta}{T + \vartheta}, \tag{9}$$

where  $\vartheta = 110.4 / (\gamma T_\infty^*)$  is normalized by the freestream temperature.

### E. Numerical methods and computational framework

The purpose of this study is to investigate the compressibility effects of Batchelor vortices on transition process. High accuracy is required for simulations of small disturbances that evolve in supersonic flows. The convective flux is evaluated using the AUSMDV scheme [37], which is classified into the advection upwind splitting method (AUSM), and the weighted essentially nonoscillatory scheme with ninth-order accuracy for the interpolation of primitive variables at cell interfaces [38–40]. The viscous flux terms are calculated to eighth-order accuracy using a central difference method. The temporal integration adopts a four-step, fourth-order accuracy scheme [41].

The physical domain is a rectangular box with sides  $L_x$ ,  $L_y$ , and  $L_z$ . The grid spacing is uniform in a space that is four times the diameter of the vortex core and centered on the vortex axis. Beyond this region, the grid splays out at irregular intervals. Note that the vortex core radius is close to the site of the maximum azimuthal velocity. The computational space is also a rectangular box composed of grids of uniform width  $\Delta \xi_i = 1$ . Supersonic inflows are introduced in the  $x$  direction and fixed Batchelor vortices for  $q = 0.16$  and  $\mu = 0.5$  or  $0.8$  with the addition of disturbance. The outflow condition at  $x = L_x$  is extrapolated to the zeroth order. To simulate an isolated vortex without a contaminated center, symmetry conditions are applied on the boundary surfaces that, except for  $y$ - $z$  planes, compose  $x$ - $y$  and  $x$ - $z$  planes; although they correspond to periodicity conditions, any induction from the other vortices is negligible under  $L_x > 40$  and  $q = 0.16$ . The Reynolds number based on the sonic velocity  $\text{Re}_M$  is 9000. Numerical simulations were performed under two thermodynamic conditions (Sec. II B).

### F. Small disturbance conditions

The spatial evolutions of Batchelor vortices were investigated under the following disturbance conditions. First, to develop linear disturbances, numerical simulations were performed for  $\mu = 0.5$  at  $M_\infty = 2.5$  and  $5.0$  with the addition of unstable modes for  $m = -1$  to  $-6$  which were obtained from an inviscid linear stability analysis. The maximum amplitude of the disturbance is set to 1 % of the mainstream flow amplitude. Although unstable modes evolving from a Batchelor vortex are classified into various types (see, for example, Refs. [42–44]), the inviscid mode arises in supersonic flows due to the high Reynolds numbers. The computational domain consists of  $L_x = 200$ ,  $L_y = L_z = 40$  and the spatial resolution is  $N_x = 601$ ,  $N_y = N_z = 251$ . Note that only for  $M_\infty = 5.0$  under a uniform stagnation temperature,  $L_x = 300$  and  $N_x = 901$  due to the late transition.

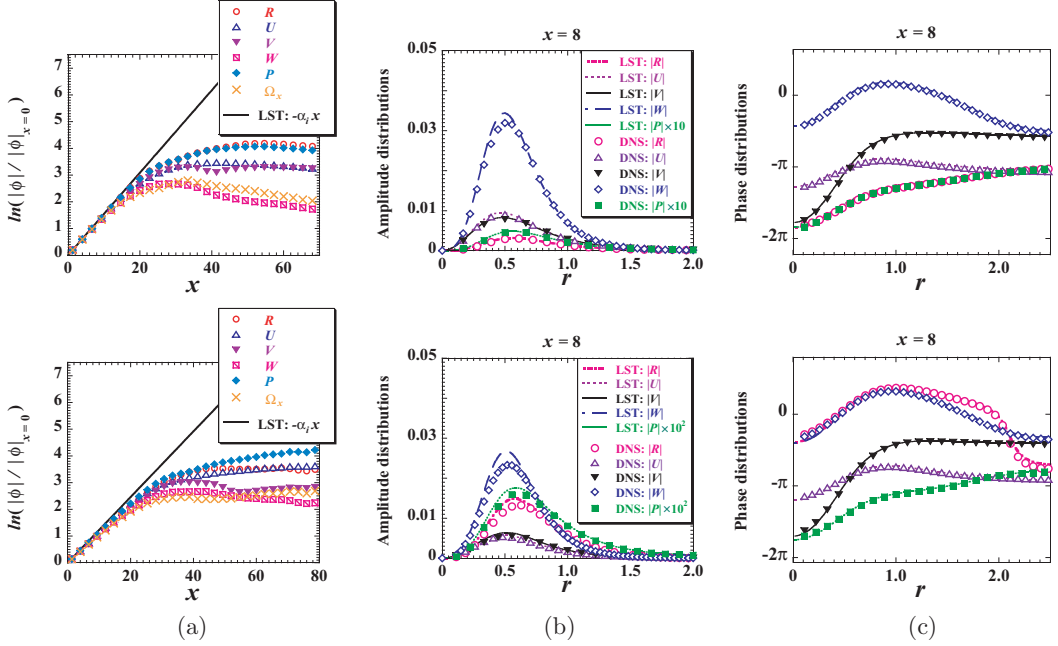


FIG. 3. Comparison of results from linear stability theory (LST) and direct numerical simulation (DNS) for eigenfunction profiles of unstable mode  $m = -3$  at  $M_\infty = 2.5$ ,  $q = 0.16$ , and  $\mu = 0.5$ ; (upper) isentropic condition, (lower) uniform stagnation temperature: (a) growth rate,  $-\alpha_i x = \ln(|\phi|/|\phi|_{x=0})$ ;  $\phi = \{R, U, V, W, P, \text{ and } \Omega_x\}$  are disturbances in the density, radial velocity, azimuthal velocity, axial velocity, pressure, and axial vorticity, respectively. (b) Amplitude and (c) phase at  $x = 8$ .

Second, to develop random disturbances, simulations were performed for  $\mu = 0.5$  and  $0.8$ . Note that random noise (white noise) whose amplitude is 3% of the mainstream flow amplitude is added. The computational domain and the resolution are  $L_x = 300$ ,  $L_y = L_z = 40$  and  $N_x = 901$ ,  $N_y = N_z = 251$ , respectively. As a compressibility parameter, the Mach number  $M_\infty$  varied among 1.5, 2.5, 3.5, and 5.0. Note that the condition  $M_\infty < 5$  satisfies the calorically perfect gas law and corresponds to a Mach number coming into the combustor of a scramjet engine, which represents approximately one third of the flight Mach number 8–15 [45]. Thus, investigating compressibility effects under these conditions is an important undertaking.

### G. Linear developments of normal modes

To clarify the linear growth of two thermodynamic profiles, Fig. 3 shows the streamwise variations in the growth rate and the eigenfunction (amplitude and phase) profiles of the disturbances obtained from the direct numerical simulation (DNS) and those obtained from the linear stability theory (LST) for  $m = -3$ . In Fig. 3(a), the growth rates obtained from DNS are consistent with those of LST (black line) during the initial growth stage. Each eigenfunction profile is very close to the linearized solution at  $x = 8$ , while the nonlinearity surfaces there. Although it is not shown here, each mean-flow profile for  $x < 16$  is in agreement with the inflow profile [30]. Thus, it is found that the numerical formulation with the high Reynolds number satisfies the solution of the inviscid linear stability analysis during the early stage. In all disturbance profiles, the amplitude of the axial velocity disturbance is the greatest, which is pronounced in the Batchelor vortex [46,47]. Large differences between the two thermodynamic profiles occur in the density disturbance. For a uniform stagnation temperature, the amplitude is the second greatest and the phase change occurs at the vortex outer edge, and for the isentropic vortex, the density disturbance is identical to the

pressure disturbance in phase, and the flow field becomes homentropic. Therefore, it is shown that the disturbance characteristic of the Batchelor vortex differs according to the thermodynamic profile.

### III. SPATIAL DEVELOPMENTS OF LINEAR UNSTABLE MODES

#### A. Effect of azimuthal wave numbers

This subsection describes the effects of azimuthal wave numbers in spatially developing Batchelor vortices with small disturbances. Figure 4 shows the isosurface of the second invariant of the velocity gradient tensor  $\mathcal{Q}$  [48], which is useful for quantitatively visualising vortical structures, for  $m = -1$  to  $-6$  at  $M_\infty = 2.5$ ,  $q = 0.16$ , and  $\mu = 0.5$ . Then, the  $\mathcal{Q}$  is given by the following equation:

$$\mathcal{Q} = \frac{1}{2}(-S_{ij}S_{ij} + R_{ij}R_{ij} + \mathcal{P}^2),$$

$$S_{ij} = \frac{1}{2} \left( \frac{\partial u_j}{\partial x_i} + \frac{\partial u_i}{\partial x_j} \right), \quad R_{ij} = \frac{1}{2} \left( \frac{\partial u_j}{\partial x_i} - \frac{\partial u_i}{\partial x_j} \right), \quad \mathcal{P} = \frac{\partial u_k}{\partial x_k}, \quad (10)$$

where  $S_{ij}$  and  $R_{ij}$  are the strain-rate and vorticity tensors, i.e., the symmetric and asymmetric components of the velocity gradient tensor  $\partial u_i/\partial x_j$ , respectively, and  $\mathcal{P}$  is the divergence of the velocity vectors. In each case, spiral (large-scale) structures, which depend on the wave number based on each unstable mode, are visible around the inflow vorticity at an early stage, as reported by Abid [42], Broadhurst and Sherwin [49]. However, the effectiveness of the thermodynamic condition on evolutions differs in Fig. 4. For  $m = -1$ , structures similar to vortex rings develop in both cases. For  $m = -2$ , vortical structures similar to a conceptual representation of a vortex breakdown described by Lambourne and Bryer [50] are shown in Figs. 4(c) and 4(d). Moreover, for  $m = -1$  and  $-2$ , isentropic cases exist small scales that are not observed in uniform stagnation-temperature cases at the downstream. For  $m = -3$  and  $-4$ , at a uniform stagnation temperature, spiral structures grow from within the vortex core [see also Fig. 5(b)], while the structures break up downstream. In contrast, the isentropic cases cause a large growth in the radial direction while the spiral structures remain as large-scale structures. For  $m = -5$  and  $-6$ , many small scales are observed downstream, compared to less than  $m = -4$ . The isentropic vortex spreads outward more than the uniform stagnation-temperature vortex; however, the difference is small compared to the results for  $m = -3$  and  $-4$ . Accordingly, it can be observed that the isentropic vortices exhibit relatively high instability in nonlinear development.

To study developing structures in planes that are perpendicular to the mainstream, Fig. 5 shows the contour lines of axial vorticity for  $m = -3$  and  $-6$  in four  $y$ - $z$  planes. Since disturbances develop as a spiral three-dimensional wave in this study, the behavior of streamwise (axial) vorticity gives a useful piece of information to us. Each development of spiral structures from within the vortex core is pronounced and occurs with accompanying reversed-sign vorticity. Note that the generation of negative axial vorticity in the  $y$ - $z$  planes could play a crucial role in large-scale bursting and assists turbulence enhancement. Since angular momentum is conserved in vortices at high Reynolds numbers, negative circulation that is related to negative vorticity increases at large positive circulation that is regarded as a local overshoot in profile. Circulation overshoot is associated with a centrifugal instability and are also required for maintaining the turbulent state [36]. Thus, negative vorticities are important for fluctuation development. The spread of uniform stagnation-temperature vortices is weak compared to that of an isentropic vortex. For the isentropic case where  $m = -3$ , three twin vortices grow clearly at  $x = 40$ , and small eddies appear in the center. In particular, the large effect of outward expansion is seen in this case [Figs. 4(e) and 5(a)]. Jacquin and Pantano [36] showed that turbulence produced within an incompressible Batchelor vortex core has to overcome a dispersion buffer that lies adjacent to the vortex core before turbulent fluctuations can reach the periphery of the vortex. Thus, the appearance of small scales in the vortex core is important for the vortex destabilisation. Furthermore, the development of the axial

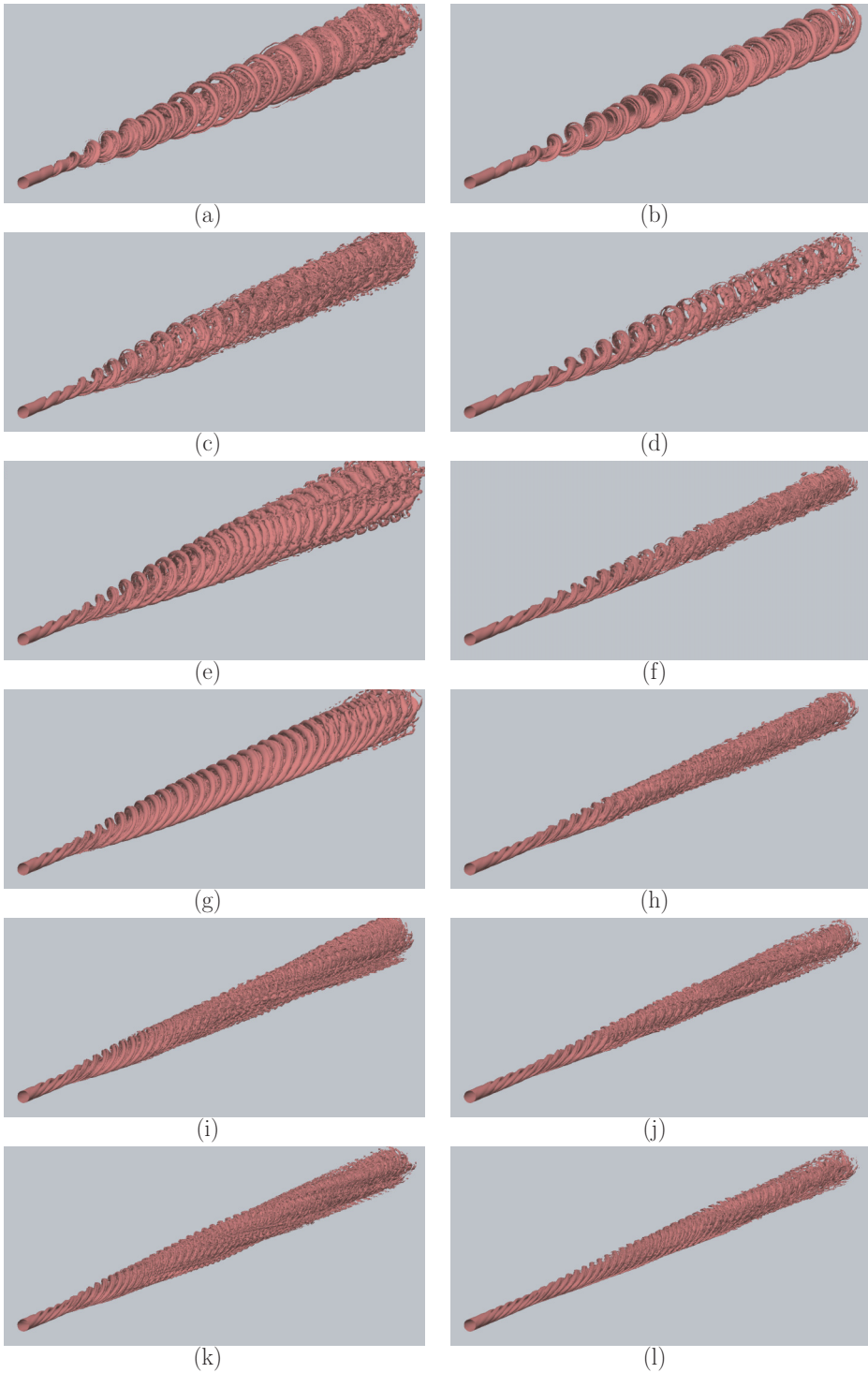


FIG. 4. Isosurfaces of the second invariant of the velocity gradient tensor  $\mathcal{Q}$  at  $M_\infty = 2.5$ ,  $q = 0.16$ , and  $\mu = 0.5$ : (left) isentropic condition and (right) uniform stagnation temperature; (a), (b)  $m = -1$ , (c), (d)  $m = -2$ , (e), (f)  $m = -3$ , (g), (h)  $m = -4$ , (i), (j)  $m = -5$ , (k), (l)  $m = -6$ .

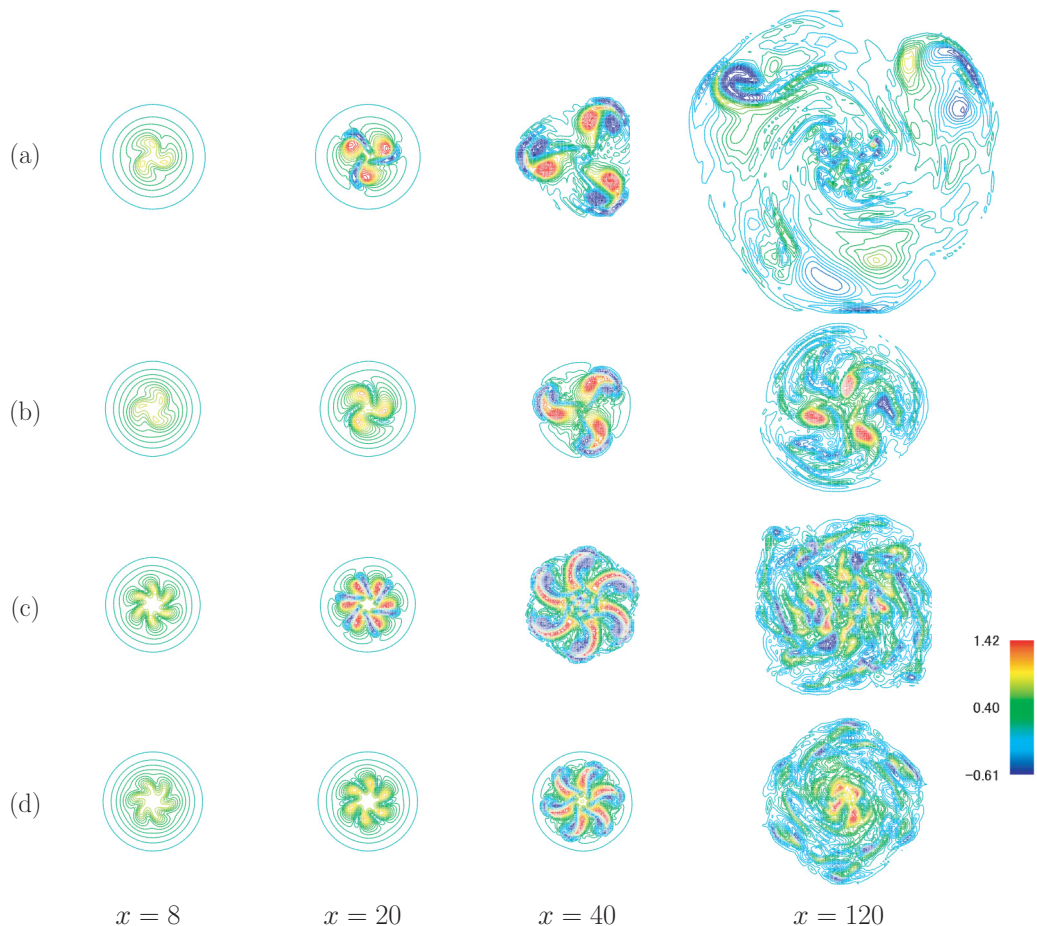


FIG. 5. Contour lines of axial vorticities  $\omega_x$  in various planes perpendicular to the axial flow: (a)  $m = -3$ , isentropic condition; (b)  $m = -3$ , uniform stagnation temperature; (c)  $m = -6$ , isentropic condition, and (d)  $m = -6$ , uniform stagnation temperature, at  $M_\infty = 2.5$ ,  $q = 0.16$ , and  $\mu = 0.5$ .

vorticity in the plane is very similar to that of the incompressible Batchelor vortex that deals with the evolution of normal modes [46]. This suggests that the compressibility effect is small in a plane perpendicular to the main flow. For  $m = -6$ , the formed spiral structures are slim and symmetrical up to  $x = 40$ . In the isentropic case, smaller structures appear in the central area of the vortex as is the case for  $m = -3$ , and such structures may trigger the collapse of the vortex downstream. Based on the  $m = -6$  results, the large-scale streamwise vortex (inflow Batchelor vortex) becomes chaotic downstream during the evolution of the high-wave-number mode. Note that, since the inflow includes only pure normal-mode disturbance, the source of such small scales could be due to a truncation error in the initial eigenfunction profiles and a high Reynolds number.

### B. Mach number effects

In this subsection, the effects of Mach number are investigated in connection with compressibility effects. First, consider the isentropic condition with the large growth rate at  $M_\infty = 5.0$  (see, Table II). In Sec. III A, the spatial evolutions show that small scales near the center are effective in the bursting. To observe the internal structures in detail, Fig. 6 shows the helicity density

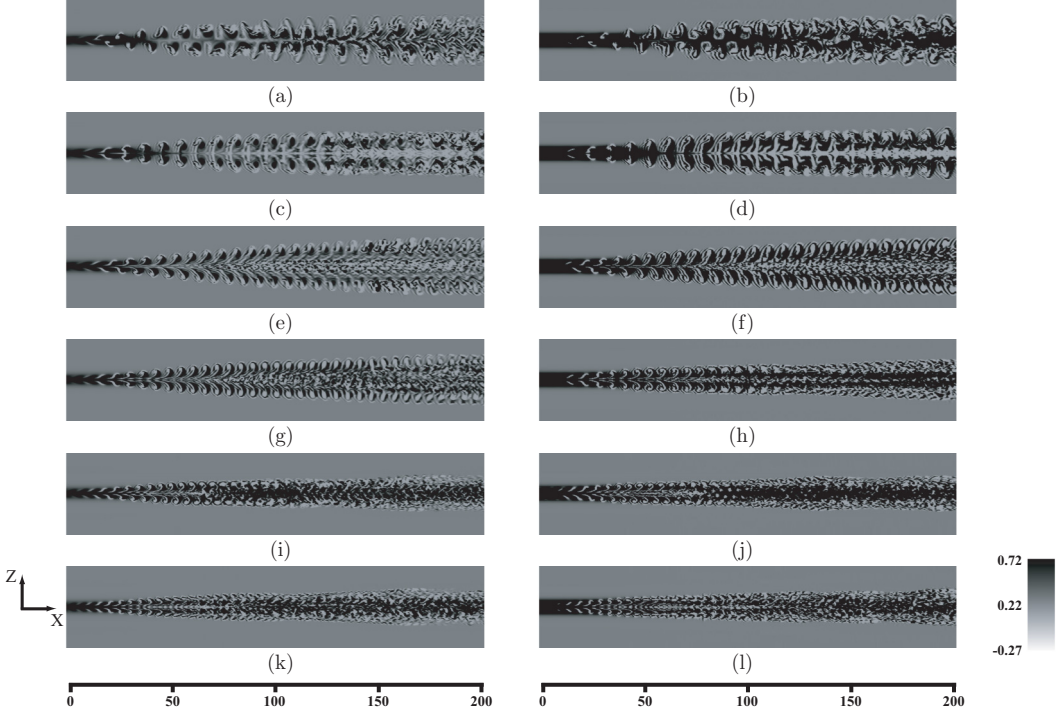


FIG. 6. Transition processes of Batchelor vortices described by helicity density contours in the cross-sections through the vortex axis: (left)  $M_\infty = 2.5$  and (right)  $M_\infty = 5.0$ ; (a), (b)  $m = -1$ , (c), (d)  $m = -2$ , (e), (f)  $m = -3$ , (g), (h)  $m = -4$ , (i), (j)  $m = -5$ , (k), (l)  $m = -6$ , for  $q = 0.16$  and  $\mu = 0.5$  under isentropic condition. Positive and negative helicities are rendered in black and white, respectively.

contours  $h = u_i \omega_i$  ( $\omega_i$  are the vorticity components) in  $x$ - $z$  cross-sections through the vortex axis at  $M_\infty = 2.5$  and  $5.0$ , and the positive and negative helicities are rendered in black and white, respectively. Helicity contours provide useful information about the transition processes of vortices [30]. In the early stage, the generated spiral structures (white) in the cross-sections are characterized as asymmetric and symmetric in response to the even-odd mode. In terms of developing structures, there is not a large difference between  $M_\infty = 2.5$  and  $5.0$  (except  $m = -4$  and over  $x \sim 150$ ). For  $m = -1$ , the feature of vortex breakdown, which the positive helicity is partly lacking on the center axis [31], is found in the contours. For  $m = -2$ , there appears to be no difference depending on the Mach number. For  $m = -3$ , the spiral structures widen outwards and small scales arise near the axis located in a gap between the spread structures, as shown in Fig. 4(e). When small scales appear in the vicinity of the vortex axis, they influence each other inside and outside the vortex, and eddies increase downstream. For  $m = -4$ , when  $M_\infty = 2.5$ , the evolution resembles that of  $m = -3$ . When  $M_\infty = 5.0$ , it is similar to that of  $m = -5$  at  $M_\infty = 2.5$ . For  $m = -5$ , the structure appears to a hybrid configuration of  $m = -4$  and  $m = -6$  (the outward spread is weak as described next). For  $m = -6$ , both  $M_\infty$  cases demonstrate that development in a plane perpendicular to the mainstream is small downstream, even under the isentropic condition. These results suggest that since the shear eddying region changes depending on the mode, the spreading rate cannot be estimated properly by using the thickness of the region, such as shear layers and no-swirling jets. In addition, it is found that compressibility effects of the isentropic vortices are weak in that the spreading rate and the fluctuation growth stay unchanged against the Mach number.

Second, consider uniform stagnation-temperature vortices. Figure 7 shows the isosurface of the second invariant of the velocity gradient tensor in Eq. (10) at  $M_\infty = 5.0$ ,  $q = 0.16$  and  $\mu = 0.5$  for

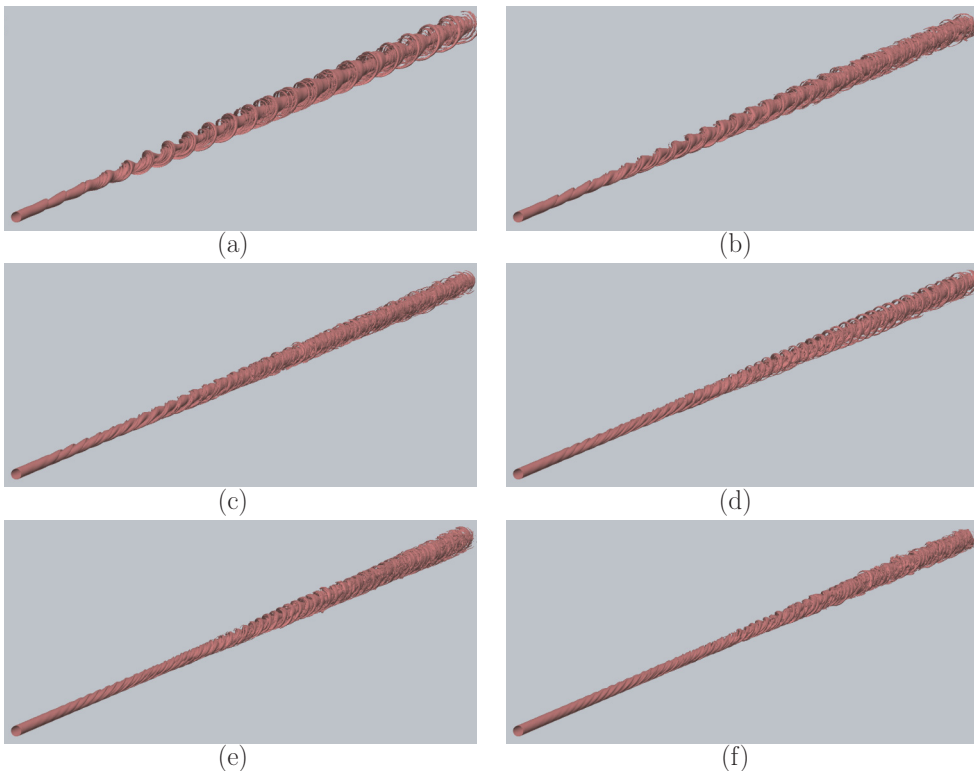


FIG. 7. Isosurfaces of second invariant of velocity gradient tensor  $\mathcal{Q}$ : (a)  $m = -1$ , (b)  $m = -2$ , (c)  $m = -3$ , (d)  $m = -4$ , (e)  $m = -5$ , (f)  $m = -6$ , at  $M_\infty = 5.0$ ,  $q = 0.16$  and  $\mu = 0.5$  under uniform stagnation temperature.

$m = -1$  to  $-6$ . In marked contrast to isentropic cases, the vortical structures differ significantly compared to those at  $M_\infty = 2.5$  in Fig. 4 (right). For each wave number, spiral structures developed around the large-scale vortices are slim and tiny, and small scales are not observable downstream. For  $m = -6$ , there is little outward extension in the radial direction, and the development might be very weak and suppressed. Thus, developments with a high wave number at high Mach numbers are passive in the vortices. Compressibility effects are most obvious on the development of uniform stagnation-temperature vortices.

#### IV. ENTROPY EFFECTS ON BATCHELOR VORTICES

##### A. Definition of fluctuation energies

Here, the compressibility effects of the Batchelor vortex are considered from a thermodynamic fluctuation perspective. One influence of the compressibility on the flow is the irreversible energy transfer process from kinetic to internal energy. Fluctuation growth is evaluated using the total fluctuation energy  $\hat{E}(= \hat{K} + \hat{P} + \hat{S})$ , which is given as follows:

$$\hat{K} = \frac{1}{2} \bar{\rho} \hat{u}_k \hat{u}_k, \quad \hat{P} = \frac{1}{2} \frac{\hat{p}^2}{\gamma \bar{p}}, \quad \hat{S} = \frac{1}{2} \frac{\bar{p}}{\gamma(\gamma - 1)} \hat{s}^2, \quad (11)$$

where the  $(-)$  and  $(\wedge)$  symbols denote the mean and fluctuating components, respectively.  $\hat{K}$  is the fluctuation kinetic energy,  $\hat{P}$  is the fluctuation pressure energy, and  $\hat{S}$  is the fluctuation entropy

energy. The entropy fluctuation is defined as

$$\hat{s} = \frac{\hat{p}}{\bar{p}} - \gamma \frac{\hat{\rho}}{\bar{\rho}}. \quad (12)$$

Note that both Eqs. (11) and (12) are derived by linear approximation [30,51,52]. According to Morkovin's hypothesis, stagnation-temperature fluctuations are expected to be negligible compared to static temperature fluctuations [10]. By assuming that pressure fluctuations are negligible, fluctuations in the thermodynamic variables can be estimated using the state of equation,  $p = \rho T$ , given as follows:

$$\frac{\hat{T}}{\bar{T}} \simeq -(\gamma - 1) \bar{M}^2 \frac{\hat{u}_x}{\bar{u}_x} = -(\gamma - 1) \frac{\bar{M}}{\bar{c}} \hat{u}_x, \quad -\frac{\hat{p}}{\bar{p}} = \frac{\hat{T}}{\bar{T}}, \quad (13)$$

where  $M$  is the local Mach number and  $c$  is the speed of sound. This relationship is derived by differentiating the conservation law of enthalpy (stagnation temperature) and is also known as the strong Reynolds analogy (SRA).

For the two thermodynamic conditions, fluctuation pressure energy  $\hat{P}$  is very weak and then  $\hat{p}$  is negligible, because pressure fluctuation  $\hat{p}$  is much smaller than the other physical fluctuations under the normalized inflow condition (Fig. 3). From Eq. (12), it is found that the entropy fluctuation corresponds to the density fluctuation in the uniform stagnation-temperature vortex. Then,  $\hat{s}$  is derived from Eq. (13) as follows:

$$\hat{s} \simeq -\gamma \frac{\hat{\rho}}{\bar{\rho}} = -\gamma (\gamma - 1) \frac{\bar{M}}{\bar{c}} \hat{u}_x. \quad (14)$$

By substituting Eq. (14) into Eq. (11) and using  $\bar{M} \simeq M_\infty$  and  $\bar{c}^2 = \gamma \bar{p}/\bar{\rho}$ , the fluctuation entropy energy  $\hat{S}$  is given as follows:

$$\hat{S} \simeq (\gamma - 1) M_\infty^2 \frac{\bar{\rho} \hat{u}_x^2}{2}. \quad (15)$$

It would be useful if this relation could be expressed by fluctuation kinetic energy  $\hat{K}$ . In a swirling flow, each component in the velocity fluctuation becomes large due to the three-dimensional effect. When the anisotropy ratios are defined as  $\hat{u}_r/\hat{u}_x$  and  $\hat{u}_\theta/\hat{u}_x$ , assume that  $\hat{u}_\theta \approx \hat{u}_r$ , and the coefficient between  $\hat{u}_x$  and  $\hat{K}$  is defined as follows:

$$\beta_K = 1 + 2 \left( \frac{\hat{u}_r}{\hat{u}_x} \right)^2. \quad (16)$$

Note that the magnitude of fluctuation in shear flows depends on the scale of the velocity deficit, differing from the boundary layer standardized by the boundary layer thickness. Using the averaged kinetic energy  $\bar{K}$  and velocity correlation  $\bar{\tau}_{0,\infty}$ , which is associated with the axial velocity deficit yielding instability in the Batchelor vortex, the following relation is obtained approximately:

$$\frac{\bar{K}}{\bar{\tau}_{0,\infty}} \simeq \frac{1}{2(1 - \mu)}, \quad (17)$$

where  $\bar{K} = \bar{\rho} \bar{u}_k(\infty) \bar{u}_k(\infty)/2$  and  $\bar{\tau}_{0,\infty} = \bar{\rho} [\bar{u}_x(0) \bar{u}_x(\infty)]$ . The average velocity correlation is similar to the reciprocal of the structure parameter [13], which denotes the ratio of the anisotropy tensor  $\overline{\hat{u}_i \hat{u}_j}$  to  $\bar{K}$ . The relationship between velocity fluctuation and the average velocity correlation based on the numerical data using random disturbances is shown in Fig. 8. Note that the vertical axis is integrated over the cross-sectional area that is perpendicular to the  $x$ -axis. The values on the vertical axis depend on the deficit  $\mu$ , and the averages of the data obtained from  $M_\infty = 1.5$  to 5.0 are close to the estimation Eq. (17). In boundary layers, the change in anisotropy due to compressibility is weak and independent of the Mach number [15]. In the vortices, from the values of  $M_\infty = 5.0$ ,

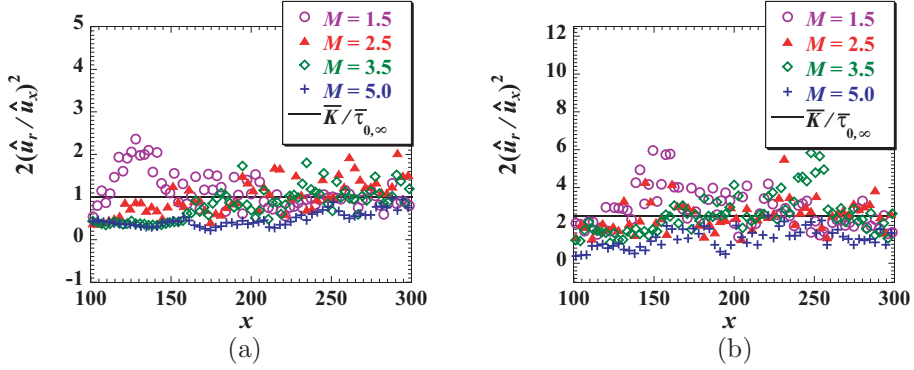


FIG. 8. Comparison of velocity fluctuation and average velocity correlation obtained from developments with random disturbances: (a)  $\mu = 0.5$  and (b)  $\mu = 0.8$ .

the anisotropy is considered to be influenced by the compressibility; however, here, it is estimated using Eq. (17). Using Eqs. (15), (16), and (17), the fluctuation entropy energy is estimated by

$$\hat{S} \simeq (\gamma - 1) M_\infty^2 \frac{\hat{K}}{\beta_K}. \quad (18)$$

This indicates that  $\hat{S}$  is compactly connected to  $\hat{K}$  based on Morkovin's hypothesis.

### B. Spatial developments of normal-mode disturbance

Figures 9 and 10 show the fluctuation energies,  $\hat{K}$ ,  $\hat{P}$ ,  $\hat{S}$  and Eq. (18) integrated over the cross-sectional area that is perpendicular to the axial flow for  $m = -1$  to  $-6$  at  $M_\infty = 2.5$  and 5.0 under uniform stagnation temperature. As discussed previously, very small pressure fluctuations are observed in these figures. Although there is no significant difference between the linear growth rates for  $m = -3$  to  $-6$  in Tables I and II, each fluctuation energy magnitude differs in the nonlinear evolutions. For  $M_\infty = 2.5$ , the fluctuation kinetic energy  $\hat{K}$  decreases as wave number  $m$  increases, and  $\hat{S}$  is comparable to  $\hat{K}$ . In terms of the fluctuation profile, Eq. (18) differs from  $\hat{S}$  at  $m = -1$  and  $-2$ . For  $m = -1$ , there are characteristic double peaks in the  $\hat{K}$  distribution. The feature of the fluctuation  $\hat{K}$  may indicate the presence of vortex breakdown. Note that vortex breakdown occurs at low wave numbers (e.g.,  $m = -1$ ) and low Mach numbers [30]. In contrast, Eq. (18) agrees with  $\hat{S}$  for  $m = -3$  to  $-6$ , where small scales are confirmed in Figs. 4(f) and 4(h). For  $M_\infty = 5.0$ ,  $\hat{S}$  is consistently greater than  $\hat{K}$ . Although  $\hat{S}$  and Eq. (18) disagree at low wave numbers ( $m = -1$  to  $-4$ ), they coincide at  $m = -5$  and  $-6$ . It also suggests that swirl-type flows, which occur a vortex breakdown and possess a compressibility relaxation, differ from shear flows in fluctuation property because large scales (i.e., low wave numbers) are often subject to the fluctuation growth in shear flows. As a result, Eq. (18) becomes consistent with  $\hat{S}$  when the wave number is high. This suggests that Morkovin's hypothesis [12] proposed in turbulent fluctuation is also applicable to the fluctuation growth of a high wave number.

To analyze small downstream structures associated with high wave numbers, the amplitudes of axial velocity disturbance decomposed by Fourier modes  $m = -1$  to  $-12$  are normalized against those of the initial added unstable modes  $m = -1, -3$ , and  $-6$  at  $M_\infty = 2.5$  (Fig. 11). The linear modes develop initially. Then, for each case, the wave numbers of the higher harmonics appear near  $x = 20$ . For example, when  $m = -3$ , the first three higher harmonics are  $-6, -9$ , and  $-12$ . For  $m = -1$ , the amplitude of high wave numbers generated downstream is low. For  $m = -6$ , the linear region is short and there is a mixture of many modes downstream. These tendencies do not contradict the fluctuation feature shown in Fig. 9, where  $\hat{S}$  matches Eq. (18) at high wave numbers.

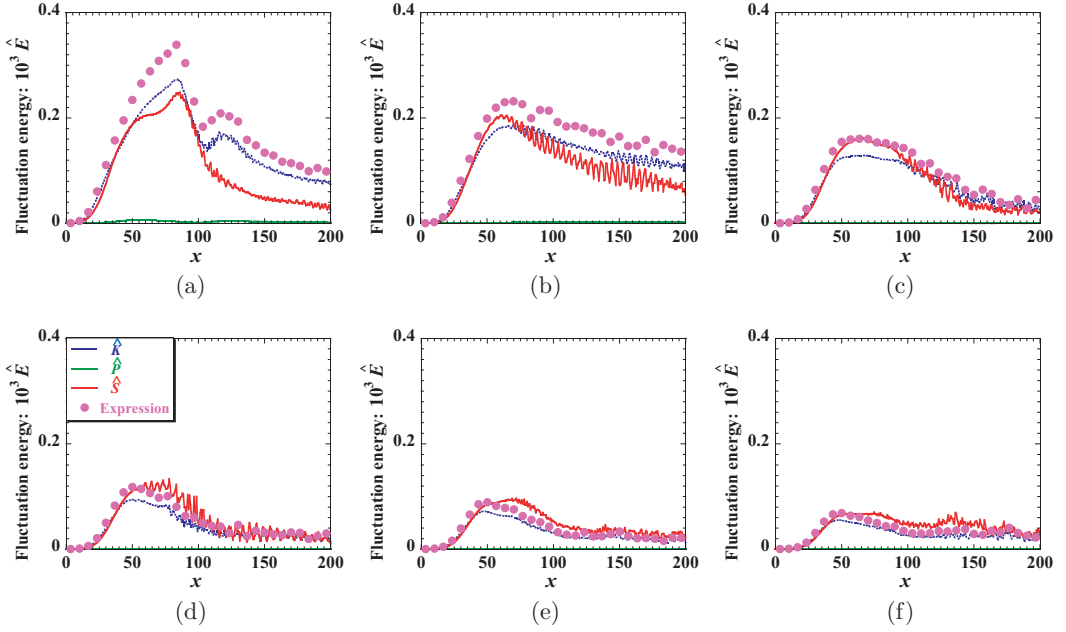


FIG. 9. Fluctuation energies of kinetic  $\hat{K}$ , pressure  $\hat{P}$ , entropy  $\hat{S}$ , and Eq. (18): (a)  $m = -1$ , (b)  $m = -2$ , (c)  $m = -3$ , (d)  $m = -4$ , (e)  $m = -5$ , (f)  $m = -6$  at  $M_\infty = 2.5$ ,  $q = 0.16$ , and  $\mu = 0.5$  under uniform stagnation temperature. Note that Eq. (18) is plotted as the closed circles.

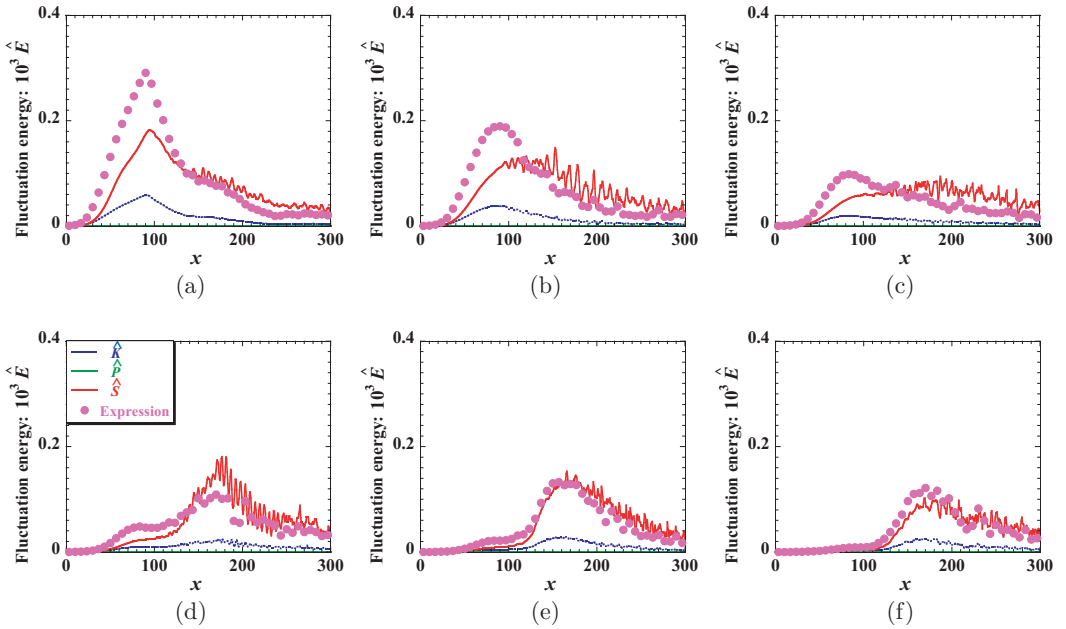


FIG. 10. Fluctuation energies of kinetic  $\hat{K}$ , pressure  $\hat{P}$ , entropy  $\hat{S}$ , and Eq. (18): (a)  $m = -1$ , (b)  $m = -2$ , (c)  $m = -3$ , (d)  $m = -4$ , (e)  $m = -5$ , (f)  $m = -6$  at  $M_\infty = 5.0$ ,  $q = 0.16$ , and  $\mu = 0.5$  under uniform stagnation temperature. Note that Eq. (18) is plotted as the closed circles.

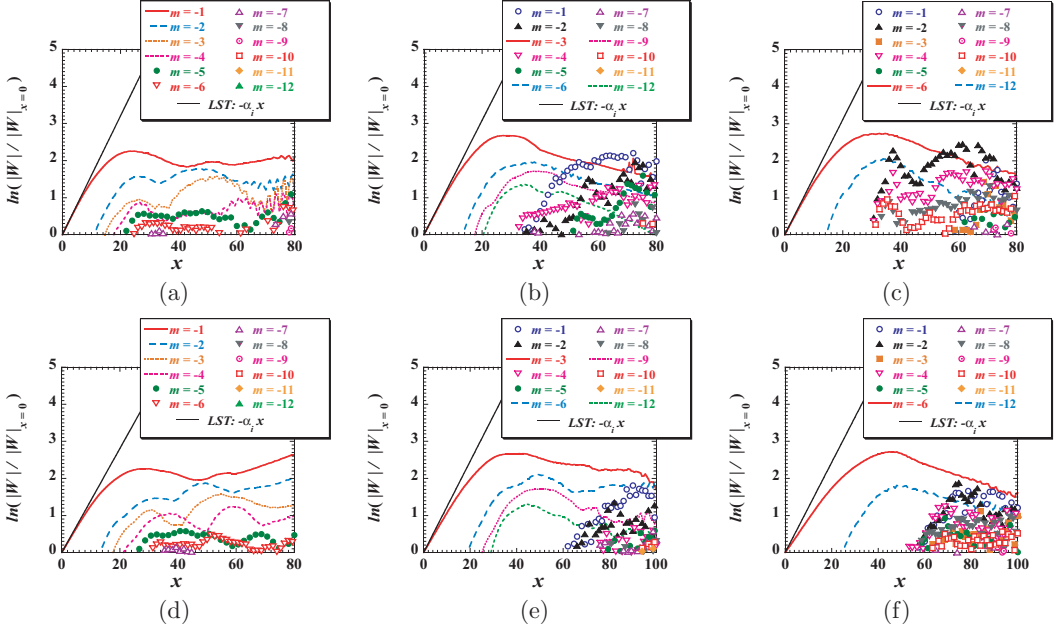


FIG. 11. Streamwise variations of normalized amplitude of axial velocity disturbance decomposed by modes  $m = -1$  to  $-12$ : (top) isentropic condition and (bottom) uniform stagnation temperature; inflow disturbance mode (a, d)  $m = -1$ , (b, e)  $m = -3$ , (c, f)  $m = -6$  for  $q = 0.16$  and  $\mu = 0.5$  at  $M_\infty = 2.5$ .

Isentropic vortices quickly create other modes in addition to the initial mode and uniform stagnation temperature vortices show that the nonlinearity that results in the emergence of other modes occurs at a relatively slower rate. These are consistent with the earlier result indicating that isentropic vortices are more unstable than uniform stagnation-temperature vortices and have the nature against compressibility effects.

### C. Spatial developments of random disturbance

In Sec. IV B, the evolutions of normal-mode disturbance indicated that, when the wave number of normal-mode is large, the feature of fluctuation energy closes in Eq. (18). It is important how different it is to evolve normal modes from random disturbances. Here, the developments of the Batchelor vortex with random disturbance are investigated for  $M_\infty = 1.5$  to 5.0.

Consider the fluctuation variables related to the evolution of random disturbance. In boundary layers, it has been reported that compressibility effects are considerable when the fluctuating Mach number is greater than 0.3 [14]. In supersonic flows, the turbulence Mach number is known as an indicator of the significance of the compressibility effects. The fluctuating Mach number  $\hat{M}$  and turbulence Mach number  $M_t$  are defined as [13]

$$\hat{M} = M - \bar{M}, \quad \bar{M} = \frac{\sqrt{\bar{u}_k \bar{u}_k}}{\bar{c}}, \quad M_t = \frac{\sqrt{\hat{u}_k \hat{u}_k}}{\bar{c}}. \quad (19)$$

Note that  $M$  denotes the local Mach number. In spatial evolution with small amplitude disturbances, the maximum  $\hat{M}$  and  $M_t$  of the Batchelor vortices are given in Table III. Overall,  $\hat{M}$  increases with increasing Mach number  $M_\infty$  and  $\hat{M} \approx 0.0355-0.0398M_\infty$ ; thus, all the  $\hat{M} < 0.3$  for small amplitude disturbance. The  $\hat{M}$  of the isentropic vortices is slightly less than that of the uniform stagnation-temperature vortices, which suggests that an increased density fluctuation of the latter vortices contributes to reduced sonic speed. Moreover, since the  $M_t$  of the former is nearly identical

TABLE III. Maximum  $\hat{M}$  and  $M_t$  in evolutions of the Batchelor vortices with small random disturbance (maximum amplitude 3% of the mainstream flow).

	$M_\infty = 1.5$	$M_\infty = 2.5$	$M_\infty = 3.5$	$M_\infty = 5.0$	$\mu$	Thermodynamic conditions
$\hat{M}/M_\infty$	0.0355	0.0373	0.0368	0.0370	0.5	Isentropic condition
$\hat{M}/M_\infty$	0.0367	0.0374	0.0388	0.0384	0.5	Uniform stagnation temperature
$\hat{M}/M_\infty$	0.0377	0.0374	0.0369	0.0395	0.8	Isentropic condition
$\hat{M}/M_\infty$	0.0378	0.0398	0.0393	0.0397	0.8	Uniform stagnation temperature
$M_t/\hat{M}$	1.0034	1.0008	1.0023	0.9823	0.5	Isentropic condition
$M_t/\hat{M}$	0.9711	0.8988	0.8613	0.8421	0.5	Uniform stagnation temperature
$M_t/\hat{M}$	1.0056	1.0109	1.0224	0.9808	0.8	Isentropic condition
$M_t/\hat{M}$	0.9531	0.8664	0.8654	0.8389	0.8	Uniform stagnation temperature

to that of the latter and is greater than the  $\hat{M}$  of the former, the fluctuation velocity is dominant. For the latter, since  $M_t$  is smaller than  $\hat{M}$ , it is suggested that density fluctuation affects the structure. Note that evolutions are heavily dependent on the intensity of initial disturbances. From a transition perspective, it is also necessary to study an evolution with larger amplitude as an initial disturbance.

For the isentropic condition, Fig. 12 shows the helicity density contours in the cross-sections through the vortex axis for  $q = 0.16$  and  $\mu = 0.8$  at  $M_\infty = 1.5$  to 5.0. At  $M_\infty = 1.5$ , vortex breakdown occurs because there are regions with no vortex on the central axis ( $L_y = L_z = 20$ ). Note that a vortex breakdown is defined as when the vortex axis disappears in a broad sense; therefore, helicity density is useful to recognize it [31]. The downstream structures at  $M_\infty = 2.5$  are similar to those in  $M_\infty = 1.5$ . Even at  $M_\infty = 3.5$ , the tendency of vortex breakdown with the downstream

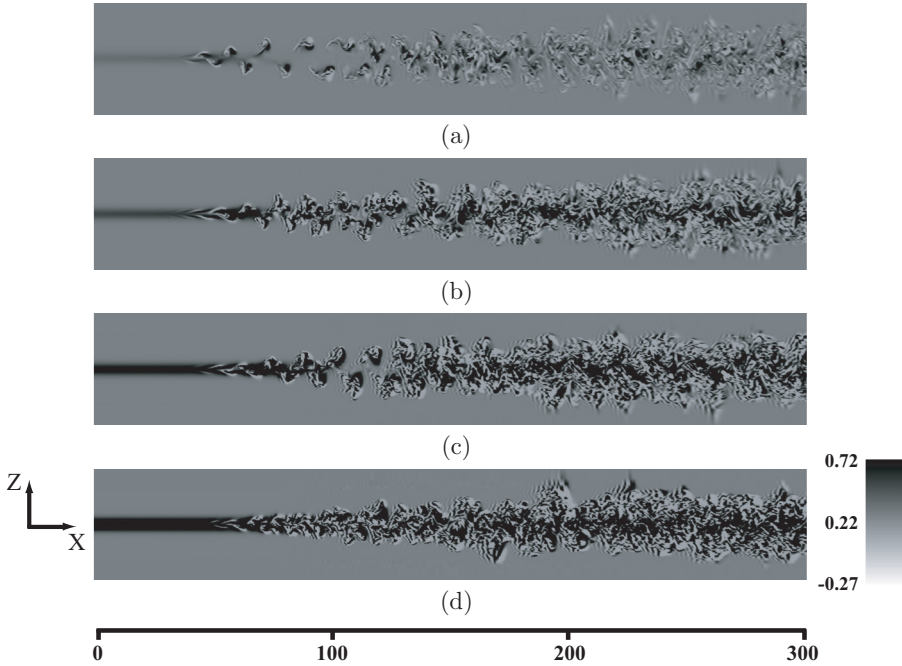


FIG. 12. Evolutions of Batchelor vortices ( $q = 0.16$ ,  $\mu = 0.8$ ) with random disturbance described by the helicity density contours in the cross-sections through the vortex axis: (a)  $M_\infty = 1.5$ , (b)  $M_\infty = 2.5$ , (c)  $M_\infty = 3.5$ , and (d)  $M_\infty = 5.0$  under isentropic condition.

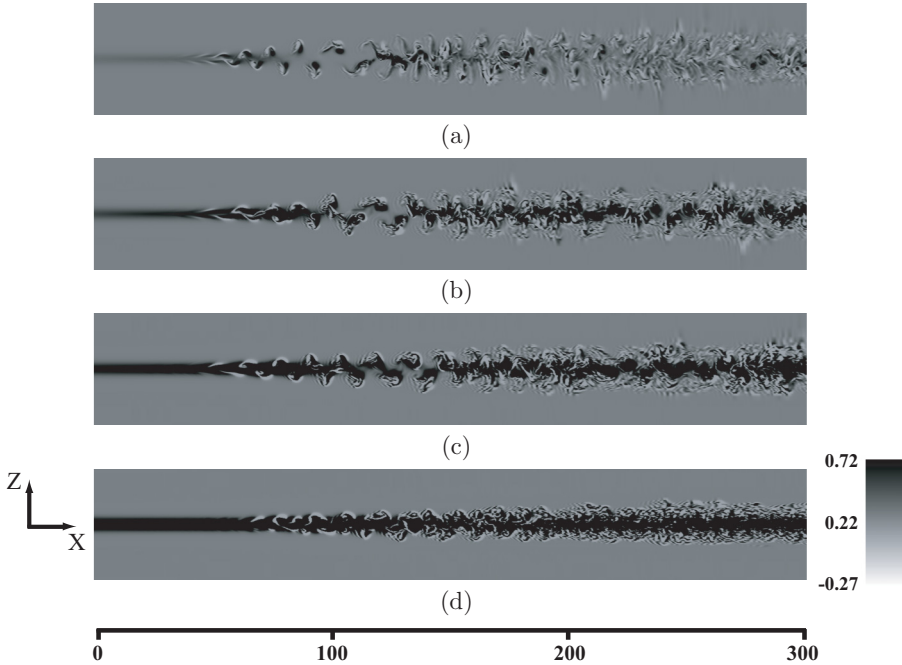


FIG. 13. Evolutions of Batchelor vortices ( $q = 0.16$ ,  $\mu = 0.8$ ) with random disturbance described by the helicity density contours in the cross-sections through the vortex axis: (a)  $M_\infty = 1.5$ , (b)  $M_\infty = 2.5$ , (c)  $M_\infty = 3.5$ , and (d)  $M_\infty = 5.0$  under uniform stagnation temperature.

small structures is observed. When  $q$  is small and  $\mu$  is large, the growth mode selected for the vortex field is  $m = -1$  based on the LST [27]. It is known that vortex breakdown is strongly related to  $m = -1$  [53]. The present results do not contradict these previous studies. It is also found that much smaller scales appear behind the vortex breakdown at the downstream. Remarkably, the outward spreading is sustained at  $M_\infty = 5.0$ , where there is an oscillation in the entire eddying region. This spreading indicates a type of entropy effect, which is related to a baroclinic property [29], because the evolution is caused by the entropy profile. For example, baroclinic vortex instabilities are present in ocean physics [54] and astrophysics [55]. In these cases, the instability is related to the global entropy gradient. The isentropic vortices exist at much smaller scales even at  $M_\infty = 5.0$ . Therefore, it is suggested that the compressibility effect weakens.

For uniform stagnation temperature, the helicity density contours in the cross-sections through the vortex axis for  $q = 0.16$  and  $\mu = 0.8$  at  $M_\infty = 1.5$  to  $5.0$  are shown in Fig. 13. At  $M_\infty = 1.5$ , vortex breakdown occurs, similar to that shown in Fig. 12(a). For  $M_\infty = 2.5$  and  $3.5$ , there is a vortical feature observed in the breakdown; however, these are low small scales compared to isentropic cases. At  $M_\infty = 5.0$ , although asymmetric vortical structures induced by the transitions develop around the Batchelor vortex, the vortex axis remains clearly downstream. Again, it is found that the spreading rates of the isentropic cases (Fig. 12) are extremely large compared to the results of the uniform stagnation-temperature vortices (Fig. 13) at high Mach numbers.

From the results shown in Fig. 13, compressibility effects are observed in uniform stagnation-temperature vortices. To study the effects from a thermodynamics fluctuation perspective, Fig. 14 plots the fluctuation energies of  $\hat{K}$ ,  $\hat{P}$ ,  $\hat{S}$  and Eq. (18) integrated over the cross-sectional area perpendicular to the axial flow for  $\mu = 0.5$  and  $0.8$ ,  $M_\infty = 1.5$ – $5.0$ . Note that all cases also result in  $\hat{P} \simeq 0$ . The results demonstrate that fluctuation kinetic energy  $\hat{K}$  decreases as  $M_\infty$  increases. In contrast, the fluctuation entropy energy  $\hat{S}$  increases with increasing  $M_\infty$  and exceeds  $\hat{K}$ . At a large

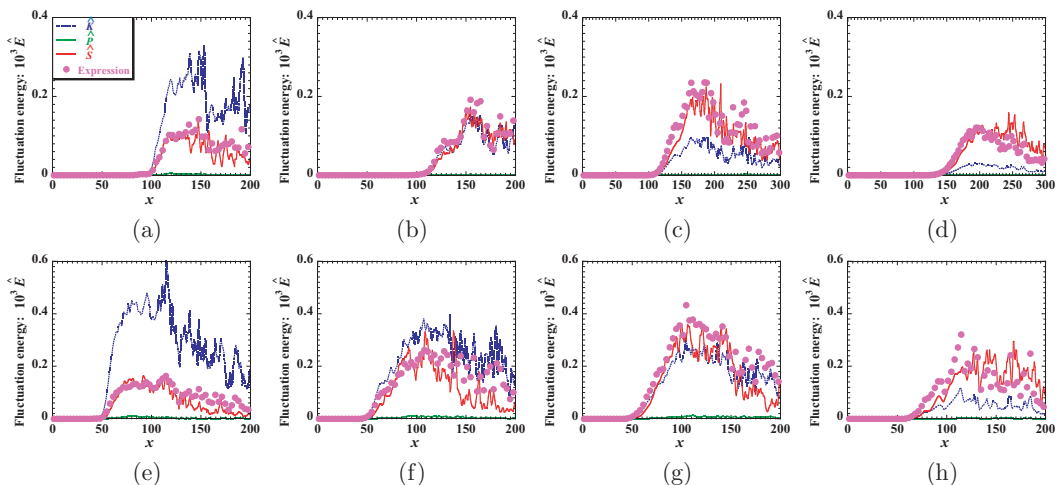


FIG. 14. Fluctuation energies of kinetic  $\hat{K}$ , pressure  $\hat{P}$ , entropy  $\hat{S}$ , and Eq. (18): (top) axial velocity deficit  $\mu = 0.5$  and (bottom)  $\mu = 0.8$ ; (a), (e)  $M_\infty = 1.5$ , (b), (f)  $M_\infty = 2.5$ , (c), (g)  $M_\infty = 3.5$ , (d), (h)  $M_\infty = 5.0$  under uniform stagnation temperature. Note that Eq. (18) is plotted as the closed circles.

Mach number, the ratio of  $\hat{S}$  to  $\hat{E}$  increases drastically. It is noteworthy that Eq. (18) based on the Morkovin's hypothesis is in good agreement with  $\hat{S}$  for each case (random disturbance evolutions). According to a recent study of thermodynamics fluctuation [56,57], the density fluctuation is the correct variable when evaluating compressibility effects. The present results also indicate that  $\hat{S}$  based on density fluctuation corresponds to compressibility strength.

#### D. Compressibility effects on Batchelor vortices

Kinetic fluctuation energy is important for turbulent growth. Using data obtained from the fluctuation energies of  $\hat{K}$ ,  $\hat{P}$ ,  $\hat{S}$  integrated over the cross-sectional area perpendicular to the axial flow, Fig. 15 plots  $\hat{K}/\hat{E}$  against  $\hat{S}/\hat{E}$  and  $M_\infty$  versus  $\hat{S}/\hat{E}$  and  $\hat{K}/\hat{E}$  for isentropic cases. As can be seen in Figs. 15(a) and 15(d), kinetic fluctuation energy  $\hat{K}$  gathers in the vicinity of  $\hat{S} \approx 0$ ; therefore,  $\hat{K} \simeq \hat{E}$ . During the evolution, entropy fluctuation energy  $\hat{S}$  is almost zero, and the  $\hat{K}/\hat{E}$  ratio is nearly equal to unity. Note that the filled circle denotes the average, and the error bar is the existence span. Both  $\hat{S}$  and  $\hat{P}$  are very small for the isentropic vortices. The nonlinear region is also subject to the initial condition  $\hat{s} = 0$ . This result is expected given that  $\hat{p}/\bar{p} = \gamma \hat{\rho}/\bar{\rho}$ , as obtained from Eq. (12). The fluctuation property  $\hat{E} \simeq \hat{K}$  is specific for energy in compressible flows, and the isentropic effect impacts nonlinear developments.

Figure 16 plots  $\hat{K}/\hat{E}$  against  $\hat{S}/\hat{E}$  and  $M_\infty$  versus  $\hat{S}/\hat{E}$  and  $\hat{K}/\hat{E}$  for uniform stagnation-temperature vortices. As Mach number  $M_\infty$  increases, entropy fluctuation energy  $\hat{S}$  increases while kinetic fluctuation energy  $\hat{K}$  decreases. In contrast to the isentropic cases, the sum of  $\hat{K}$  and  $\hat{S}$  is constant as shown in Figs. 16(a) and 16(d). The present results satisfy the following:

$$\hat{K} \simeq \hat{E} - \hat{S}. \quad (20)$$

The entropy effect observed in the linear stability analysis [27] is operative in nonlinear regions. Since an increase in entropy fluctuation correlates with decreased kinetic fluctuation energy, this result represents the compressibility effect based on entropy fluctuation.

Consider the characteristics of  $\hat{K}$  against Mach number  $M_\infty$ . Here, the results shown in Figs. 15 and 16 are summarized using Mach number  $M_0^*$  as described in Eq. (21). Figure 17 shows the ratio of  $\hat{K}$  to  $\hat{E}$  as a function of  $M_0^*$  for the isentropic and uniform stagnation-temperature vortices. The pressure fluctuations are negligibly small for the two thermodynamic conditions. For the isentropic

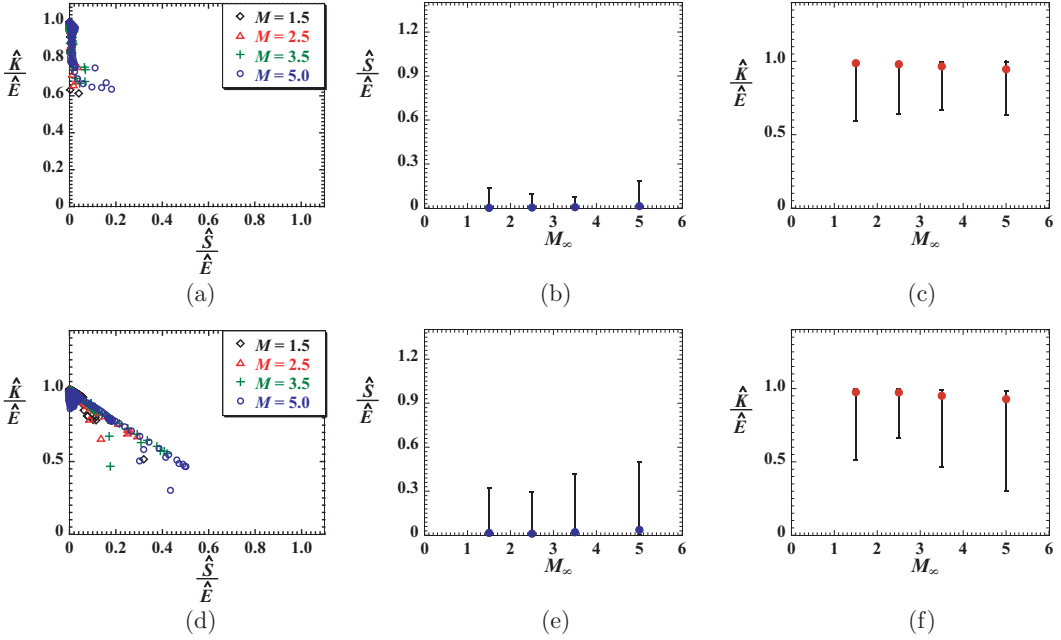


FIG. 15. Isentropic conditions: (top) the axial velocity deficit  $\mu = 0.5$  and (bottom)  $\mu = 0.8$ ; (a, d)  $\hat{S}/\hat{E}$  (ratio of entropy  $\hat{S}$  to total  $\hat{E}$ ) versus  $\hat{K}/\hat{E}$  (ratio of kinetic  $\hat{K}$  to total  $\hat{E}$ ), (b), (e)  $M_\infty$  versus  $\hat{S}/\hat{E}$ , (c), (f)  $M_\infty$  versus  $\hat{K}/\hat{E}$  (the filled circle denotes the average and the error bar indicate the existence span).

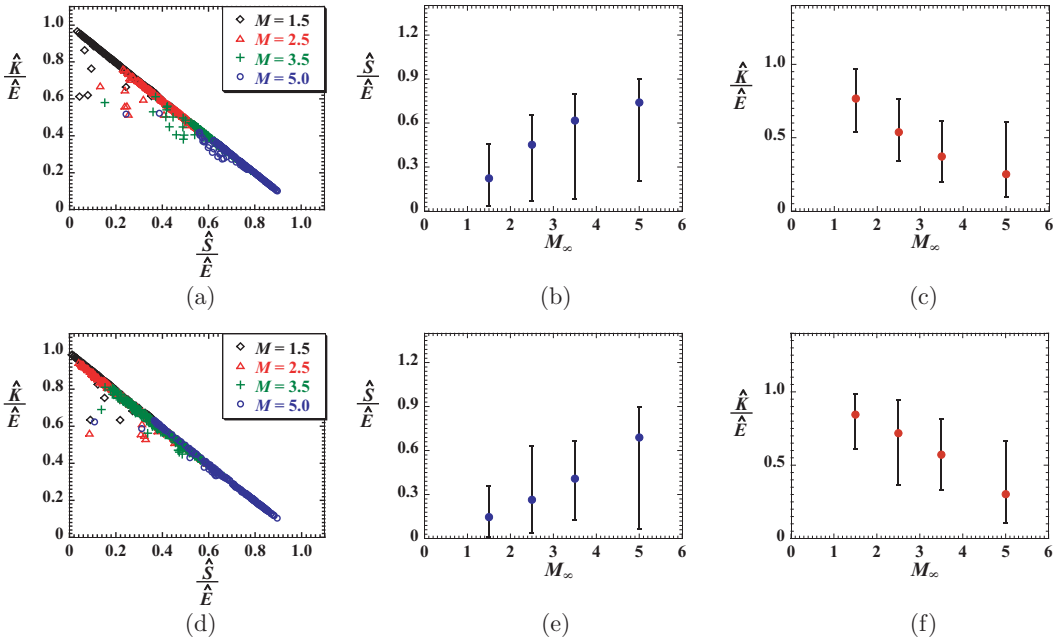


FIG. 16. Uniform stagnation-temperature conditions: (top) the axial velocity deficit  $\mu = 0.5$  and (bottom)  $\mu = 0.8$ ; (a, d)  $\hat{S}/\hat{E}$  (ratio of entropy  $\hat{S}$  to total  $\hat{E}$ ) versus  $\hat{K}/\hat{E}$  (ratio of kinetic  $\hat{K}$  to total  $\hat{E}$ ), (b), (e)  $M_\infty$  versus  $\hat{S}/\hat{E}$ , (c, f)  $M_\infty$  versus  $\hat{K}/\hat{E}$  (the filled circle denotes the average and the error bar indicate the existence span).

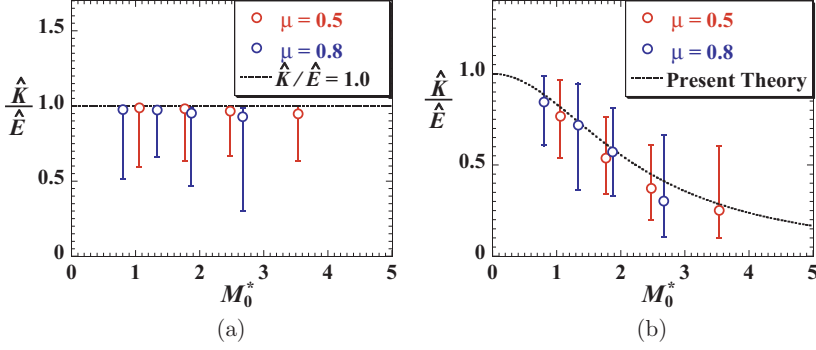


FIG. 17. Ratio of  $\hat{K}$  to  $\hat{E}$  and the theoretical curves Eqs. (20) and (21) as a function of  $M_0^*$ ; (a) isentropic vortices and (b) uniform stagnation-temperature vortices (the circle denotes the average and the error bar indicates the existence span).

cases, the ratio of  $\hat{K}/\hat{E}$  against  $M_0^*$  is almost unity, except that it decreases slightly at  $M_\infty = 5.0$ . Thus,  $\hat{K}$  is unaffected by the Mach number. For the uniform stagnation-temperature cases, the  $\hat{K}/\hat{E}$  ratio decreases with increasing  $M_0^*$ . Eliminating  $\hat{S}$  from Eqs. (18) and (20), we derive the following:

$$\frac{\hat{K}}{\hat{E}} \simeq \frac{1}{1 + \frac{\gamma-1}{2} M_0^{*2}}, \quad (21)$$

where  $M_0^* = M_\infty / \sqrt{\beta_K}$ . Note that  $\beta_K$  depends on the velocity deficit  $\mu$ . The curve obtained from Eq. (21) is consistent with the average values of  $\hat{K}/\hat{E}$  described by the circle in Fig. 17(b). From an analogy perspective, this feature is similar to the relation between the convective Mach number and the growth rate [2,6,8,27]. Moreover, when the velocity deficit is large, compressibility weakens.

Suitable scaling factors are required to compare different results that represent compressibility effects. As mentioned previously, isentropic vortices only exhibit fluctuating kinetic energy, and uniform stagnation-temperature vortices exhibit large entropy and small kinetic fluctuations as the Mach number increases. To summarize the results of isentropic and uniform stagnation-temperature vortices using the fluctuation averaged values, Fig. 18 plots  $\hat{K}/\hat{E}$  against  $\hat{S}/\hat{E}$  with the two thermodynamic conditions. The kinetic fluctuation energy  $\hat{K}$  corresponds to fluctuation growth and entropy fluctuation energy  $\hat{S}$  expresses the degree of compressibility. In this relationship, total fluctuation energy  $\hat{E}$  is saved as the sum of  $\hat{K}$  and  $\hat{S}$ . Compressibility effects arise from irreversible

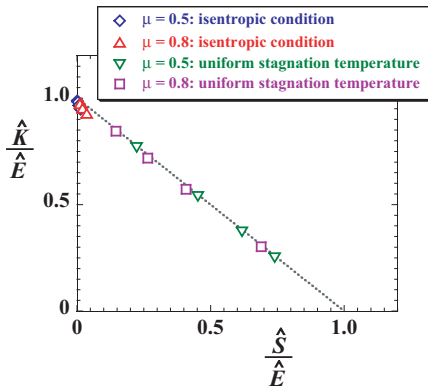


FIG. 18.  $\hat{S}/\hat{E}$  versus  $\hat{K}/\hat{E}$  plotted using the average value of each case.

transfer from kinetic to internal energies. In developments, entropy fluctuation energy  $\hat{S}$  does not occur in isentropic vortices and increases in uniform stagnation-temperature vortices. Therefore, from the energy transfer, it follows that the entropy fluctuation reflects the compressibility effect appropriately.

## V. CONCLUDING REMARKS

Previous studies have indicated that supersonic streamwise vortices are not susceptible to compressibility effects in aerospace applications [21–23,27]. Unlike basic shear flows, since streamwise vortices have a crossflow component with the mainstream, the produced fluctuations are transferred to the radial direction perpendicular to the main flow. Thus, it is easy to assume that compressibility can be avoided. However, despite considerable research, little is known about the mechanism and main factors of instability suppression, which are caused by an increased Mach number. In previous studies of boundary layers and shear layers [13], it was suggested that compressibility effects are associated with thermodynamic profiles and fluctuations in compressible flows. The subject of this paper is to clarify the effect that the thermodynamic properties of streamwise vortices have on compressibility effects. The spatial evolutions and compressibility effects of supersonic Batchelor vortices with small disturbances were investigated for various Mach numbers. In terms of thermodynamic properties of Batchelor vortices, isentropic and uniform stagnation-temperature vortices were examined.

In the evolutions of linear unstable modes (from  $m = -1$  to  $-6$ ), spiral structures based on each unstable mode appeared around the inflow Batchelor vortex. The effectiveness of the thermodynamic condition on evolutions differed depending on the wave number and Mach number. In particular, the development of the isentropic vortex with  $m = -3$  spread outward and gave rise to small scales near the axis such that the spreading rate was significantly large. For uniform stagnation-temperature cases, developments with a high wave number at high Mach numbers were weak in the vortices. Since the shear eddying region changes depending on the inflow thermodynamic property and the unstable mode, the spreading rate of Batchelor vortices cannot be estimated by the thickness of the region. This stands in contrast to shear layers and no-swirling jets. In the developments of random disturbances, vortex breakdown occurs at low Mach numbers in both thermodynamic conditions, and small scales appear behind the breakdown at the downstream. Figure 2 shows that the difference between most unstable modes to each normal mode  $m$  is very small and plural modes have a possibility of competing in white noise. Note that the growth rate for  $|m| = 1$  is slightly large in both the conditions. This may be a factor that vortex breakdown occurs in developments of random disturbances. For isentropic cases, the difference in developing vortical structures is small in response to an increased Mach number. From vortical structures, it is observed that isentropic vortices exist at much smaller scales and larger spreading rates than the uniform stagnation-temperature vortices at a high Mach number. Thus, it follows that the isentropic vortices are not subject to compressibility effects, and the uniform stagnation-temperature vortices are suppressed in vortical growth with increasing Mach number.

Compressibility effects of the Batchelor vortex with nonuniform thermodynamic profiles were considered from a thermodynamic fluctuation perspective. In spatial developments, the property of fluctuation energies indicates that the isentropic vortices only exhibited kinetic energy fluctuation and that uniform stagnation-temperature vortices yielded large entropy fluctuation in the total fluctuation energy. For uniform stagnation-temperature cases, the increase in entropy fluctuations was associated with reduced kinetic fluctuation energy and evolution of the Batchelor vortices was affected by the compressibility effects based on the fluctuation properties. As a result, a feature of compressibility effects was expressed correctly by the entropy fluctuation obtained from the density fluctuation. This is consistent with the analysis of compressible turbulence by Gerolymos and Vallet [57] in that the compressibility is strongly related to the density (entropy) fluctuation. In addition, it was found that the entropy fluctuation property at uniform stagnation temperatures can be estimated from the fluctuation kinetic energy using the expression derived from Morkovin's hypothesis [12],

which is primarily applied to compressible boundary layers. This result will be useful relative to evaluating the degree of compressibility in flows with near uniform stagnation temperatures. For example, the expression is expected to be valuable for supersonic jets that frequently employ the Crocco–Busemann relation [58], which is close to a uniform stagnation temperature. The finding highlights the fact that the kinetic fluctuation energy corresponds to the degree of disturbance growth and that the entropy fluctuation energy expresses the degree of compressibility. Therefore, the present study provides important results that are expected to lead to clarification of universal compressibility effects to flow fields with nonuniform thermodynamic profiles.

In a vortex evolution under the isentropic condition obtained as a rigorous solution of Euler’s equation, the kinetic fluctuation energy does not contribute remarkably to the internal fluctuation energy. If we could obtain a vortex with an isentropic profile, then the compressibility effect, i.e., reduction in the disturbance growth as the Mach number increases, should be reduced as described above. Exploring why the connection between kinetic fluctuation and thermodynamic fluctuation becomes weak in such a homentropic flow will be the focus of future work.

### ACKNOWLEDGMENTS

This work was partly achieved through the use of large-scale computer systems SX-ACE at the Cybermedia Center, Osaka University and was supported by JSPS KAKENHI Grant No. JP17K05145. The author expresses his gratitude to the anonymous referees for helping to improve the paper.

### APPENDIX: GRID INDEPENDENCE STUDY

To check the resolution, the following results were compared between four grids: (grid A)  $601 \times 87 \times 87$ , (grid B)  $601 \times 121 \times 121$ , (grid C)  $601 \times 171 \times 171$ , and (grid D)  $601 \times 251 \times 251$ . Figure 19 shows the streamwise variations in the growth rate of the axial velocity disturbance  $W$  and the spatial developments of  $\hat{E}$  for an isentropic vortex with  $m = -6$  at  $M_\infty = 2.5$ . In terms of evolution of the normal mode, there was little difference between grid C and grid D and the growth rate was in agreement with the spatial growth rate of the inviscid LST during the initial stage. In terms of total fluctuation energy, although the peak values of grid A and grid B are lower than others, there is not a large difference between grid C and grid D during the nonlinear development. Thus, more than resolution of grid C was reasonable in spatial evolutions.

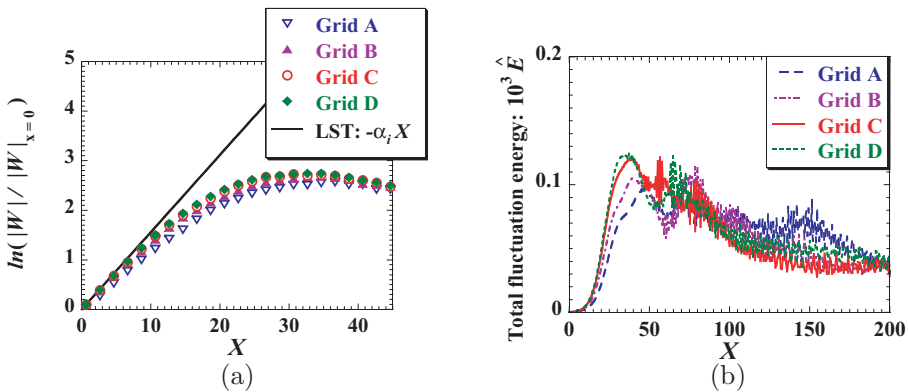


FIG. 19. Streamwise variations in the growth rate for the unstable mode  $m = -6$  at  $M_\infty = 2.5$ ,  $q = 0.16$ , and  $\mu = 0.5$ ; (a) axial velocity disturbance  $W$  and (b) total fluctuation energies  $\hat{E}$ .

- [1] G. L. Brown and A. Roshko, On density effects and large structure in turbulent mixing layers, *J. Fluid Mech.* **64**, 775 (1974).
- [2] D. Bogdanoff, Compressibility effects in turbulent shear layers, *AIAA J.* **21**, 926 (1983).
- [3] D. Papamoschou and A. Roshko, The compressible turbulent shear layer experimental study, *J. Fluid Mech.* **197**, 453 (1988).
- [4] N. T. Clemens and M. G. Mungal, Large-scale structure and entrainment in the supersonic mixing layer, *J. Fluid Mech.* **284**, 171 (1995).
- [5] P. E. Dimotakis, Turbulent free shear layer mixing and combustion, In *High Speed Flight Propulsion Systems*, Vol. 137, Chap. 5. Progress in Astronautics and Aeronautics, edited by S. Murthy and E. Curran (AIAA, Washington, 1991), pp. 265–340.
- [6] M. D. Slessor, M. Zhuang, and P. E. Dimotakis, Turbulent shear-layer mixing: Growth-rate compressibility scaling, *J. Fluid Mech.* **414**, 35 (2000).
- [7] S. Barre, C. Quine, and J. P. Dussauge, Compressibility effects on the structure of supersonic mixing layers: Experimental results, *J. Fluid Mech.* **259**, 47 (1994).
- [8] A. W. Vreman, N. D. Sandham, and K. H. Luo, Compressible mixing layer growth rate and turbulence characteristics, *J. Fluid Mech.* **320**, 235 (1996).
- [9] C. Pantano and S. Sarkar, A study of compressibility effects in the high-speed turbulent shear layer using direct simulation, *J. Fluid Mech.* **451**, 329 (2002).
- [10] P. Bradshaw, Compressible turbulent shear layers, *Annu. Rev. Fluid Mech.* **9**, 33 (1977).
- [11] S. K. Lele, Compressibility effects on turbulence, *Annu. Rev. Fluid Mech.* **26**, 211 (1994).
- [12] M. V. Morkovin, Effects of compressibility on turbulent flows, In *Mécanique de la Turbulence*, edited by A. Favre (Centre National de la Recherche Scientifique, 1962), pp. 367–380.
- [13] A. J. Smits and J.-P. Dussauge, *Turbulent Shear Layers in Supersonic Flow*, 2nd ed. (Springer Science & Business Media, Berlin, 2006).
- [14] E. F. Spina, A. J. Smits, and S. K. Robinson, The physics of supersonic turbulent boundary layers, *Annu. Rev. Fluid Mech.* **26**, 287 (1994).
- [15] L. Duan, I. Beekman, and M. P. Martín, Direct numerical simulation of hypersonic turbulent boundary layers. Part 3. Effect of Mach number, *J. Fluid Mech.* **672**, 245 (2011).
- [16] S. A. Lutz, Modeling of density fluctuations in supersonic turbulent boundary layer, *AIAA J.* **27**, 822 (1989).
- [17] G. A. Gerolymos and I. Vallet, Pressure, density, temperature and entropy fluctuations in compressible turbulent plane channel flow, *J. Fluid Mech.* **757**, 701 (2014).
- [18] K. Liu and R. H. Pletcher, Compressibility and variable density effects in turbulent boundary layers, *J. Heat Transfer* **129**, 441 (2006).
- [19] M. E. Goldstein, Turbulence generated by the interaction of entropy fluctuations with non-uniform mean flows, *J. Fluid Mech.* **93**, 209 (1979).
- [20] K. C. Schadow, E. Gutmark, and K. J. Wilson, Compressible spreading rates of supersonic coaxial jets, *Exp. Fluids* **10**, 161 (1990).
- [21] E. J. Gutmark, K. C. Schadow, and K. H. Yu, Mixing enhancement in supersonic free shear flows, *Annu. Rev. Fluid Mech.* **27**, 375 (1995).
- [22] G. S. Settles, Supersonic mixing enhancement by vorticity for high-speed propulsion (1991), NASA CR–188920.
- [23] I. A. Waitz, Y. J. Qiu, T. A. Manning, A. K. S. Fung, J. K. Elliot, J. M. Kerwin, J. K. Krasnodebski, M. N. O’Sullivan, D. E. Tew, E. M. Greitzer, F. E. Marble, C. S. Tan, and T. G. Tillman, Enhanced mixing with streamwise vorticity, *Prog. Aerospace Sci.* **33**, 323 (1997).
- [24] N. D. Sandham and W. C. Reynolds, Three-dimensional simulations of large eddies in the compressible mixing layer, *J. Fluid Mech.* **224**, 133 (1991).
- [25] L. Parras and S. Le Dizés, Temporal instability modes of supersonic round jets, *J. Fluid Mech.* **662**, 173 (2010).
- [26] J. W. Naughton, L. N. Cattafesta, and G. S. Settles, An experimental study of compressible turbulent mixing enhancement in swirling jets, *J. Fluid Mech.* **330**, 271 (1997).
- [27] T. Hiejima, Linear stability analysis on supersonic streamwise vortices, *Phys. Fluids* **25**, 114103 (2013).

- [28] T. Hiejima, Spatial evolution of supersonic streamwise vortices, *Phys. Fluids* **26**, 074102 (2014).
- [29] T. Hiejima, Stability of compressible streamwise vortices, *Phys. Fluids* **27**, 074107 (2015).
- [30] T. Hiejima, Streamwise vortex breakdown in supersonic flows, *Phys. Fluids* **29**, 054102 (2017).
- [31] T. Hiejima, Onset conditions for vortex breakdown in supersonic flows, *J. Fluid Mech.* **840**, R1 (2018).
- [32] G. K. Batchelor, Axial flow in trailing line vortices, *J. Fluid Mech.* **20**, 645 (1964).
- [33] S. V. Alekseenko, P. A. Kuibin, and V. L. Okulov, *Theory of Concentrated Vortices. An Introduction* (Springer, Berlin, 2007).
- [34] S. I. Green, *Fluid Vortices* (Kluwer, Dordrecht, 1995).
- [35] T. Hiejima, Theoretical analysis of streamwise vortex circulation induced by a strut injector, *Phys. Rev. Fluids* **1**, 054501 (2016).
- [36] L. Jacquin and C. Pantano, On the persistence of trailing vortices, *J. Fluid Mech.* **471**, 159 (2002).
- [37] Y. Wada and M.-S. Liou, A flux splitting scheme with high-resolution and robustness for discontinuities (1994), AIAA Paper No. 94–0083.
- [38] R. Borges, M. Carmona, B. Costa, and W. S. Don, An improved weighted essentially non-oscillatory scheme for hyperbolic conservation laws, *J. Comput. Phys.* **227**, 3191 (2008).
- [39] X. Deng and H. Zhang, Developing high-order weighted compact nonlinear schemes, *J. Comput. Phys.* **165**, 22 (2000).
- [40] T. Nonomura and K. Fujii, Robust explicit formulation of weighted compact nonlinear scheme, *Comp. Fluids* **85**, 8 (2013).
- [41] A. Jameson, W. Schmidt, and E. Turkel, Numerical simulation of the Euler equations by finite volume method using Runge–Kutta time stepping schemes (1981), AIAA paper No. 81–1259.
- [42] M. Abid, Nonlinear mode selection in a model of trailing line vortices, *J. Fluid Mech.* **605**, 19 (2008).
- [43] C. J. Heaton, J. W. Nichols, and P. J. Schmid, Global linear stability of the non-parallel Batchelor vortex, *J. Fluid Mech.* **629**, 139 (2009).
- [44] M. Lessen, P. J. Singh, and F. Paillet, The stability of a trailing line vortex. Part 1. Inviscid theory, *J. Fluid Mech.* **63**, 753 (1974).
- [45] T. Hiejima, Effects of streamwise vortex breakdown on supersonic combustion, *Phys. Rev. E* **93**, 043115 (2016).
- [46] I. Delbende and M. Rossi, Nonlinear evolution of a swirling jet instability, *Phys. Fluids* **17**, 044103 (2005).
- [47] M. Khorrani and C. Chang, Linear and nonlinear evolution of disturbances in supersonic streamwise vortices (1997), AFOSR–TR–97.
- [48] J. Jeong and F. Hussain, On the identification of a vortex, *J. Fluid Mech.* **285**, 69 (1995).
- [49] M. S. Broadhurst and S. J. Sherwin, Helical instability and breakdown of a Batchelor trailing vortex, In *Prog. in Industrial Mathematics at ECMI 2006. Mathematics in Industry* (Springer, Berlin, 2008), pp. 191–195.
- [50] N. C. Lambourne and D. W. Bryer, The bursting of leading-edge vortices—Some observations and discussion of the phenomenon, *Aero. Res. Counc. R&M* **3282** (1961).
- [51] A. Hanifi, P. J. Schmid, and D. S. Henningson, Transient growth in compressible boundary layer flow, *Phys. Fluids* **8**, 826 (1996).
- [52] L. M. Mack, Boundary layer stability theory, *JPL Report No. 900–277* (1969).
- [53] U. A. Qadri, D. Mistry, and M. P. Juniper, Structural sensitivity of spiral vortex breakdown, *J. Fluid Mech.* **720**, 558 (2013).
- [54] P. M. Saunders, The instability of a baroclinic vortex, *J. Phys. Oceanogr.* **3**, 61 (1973).
- [55] N. Raettig, W. Lyra, and H. Klahr, A parameter study for baroclinic vortex amplification, *ApJ* **765**, 115 (2013).
- [56] D. A. Donzis and S. Jagannathan, Fluctuations of thermodynamic variables in stationary compressible turbulence, *J. Fluid Mech.* **733**, 221 (2013).
- [57] G. A. Gerolymos and I. Vallet, Correlation coefficients of thermodynamic fluctuations in compressible aerodynamic turbulence, *J. Fluid Mech.* **851**, 447 (2018).
- [58] H. Schlichting, *Boundary-Layer Theory: 7th Edition* (McGraw-Hill, New York, 1979).